7-28-2011

Ice-Bed Coupling Beneath and Beyond Ice Streams: Byrd Glacier, Antarctica

Terence J. Hughes
University of Maine - Main, terry.hughes@maine.edu

Aitbala Sargent

James L. Fastook

Ice-bed coupling beneath and beyond ice streams: Byrd Glacier, Antarctica

Terence Hughes,[1] Aitbala Sargent,[2] and James Fastook[2]

Received 11 October 2010; revised 25 March 2011; accepted 18 April 2011; published 28 July 2011.

[1] Ice sheet thickness is determined mainly by the strength of ice-bed coupling that controls holistic transitions from slow sheet flow to fast streamflow to buttressing shelf flow. Byrd Glacier has the largest ice drainage system in Antarctica and is the fastest ice stream entering Ross Ice Shelf. In 2004 two large subglacial lakes at the head of Byrd Glacier suddenly drained and increased the terminal ice velocity of Byrd Glacier from 820 m yr^{-1} to 900 m yr^{-1}. This resulted in partial ice-bed recoupling above the lakes and partial decoupling along Byrd Glacier. An attempt to quantify this behavior is made using flowband and flowline models in which the controlling variable for ice height above the bed is the floating fraction ϕ of ice along the flowband and flowline. Changes in ϕ before and after drainage are obtained from available data, but more reliable data in the map plane are required before Byrd Glacier can be modeled adequately. A holistic sliding velocity is derived that depends on ϕ, with contributions from ice shearing over coupled beds and ice stretching over uncoupled beds, as is done in state-of-the-art sliding theories.

Citation: Hughes, T., A. Sargent, and J. Fastook (2011), Ice-bed coupling beneath and beyond ice streams: Byrd Glacier, Antarctica, *J. Geophys. Res.*, *116*, F03005, doi:10.1029/2010JF001896.

1. Introduction

[2] We seek to determine the strength of ice-bed coupling beneath and beyond Byrd Glacier that decreases from sheet to stream to shelf flow. Byrd Glacier has the largest ice drainage system on the planet (Figure 1). It drains about ten percent of the East Antarctic Ice Sheet [*Rignot and Thomas*, 2002]. Byrd Glacier occupies a fjord 100 km long through the Transantarctic Mountains, and becomes afloat halfway along the fjord before entering Ross Ice Shelf at 80.5°S, 160°E. Fast streamflow develops from tributaries in strongly converging sheet flow beyond the fjord headwall. *Stearns et al.* [2008] reported that velocity in Byrd Glacier increased by ten percent, from 820 m yr^{-1} to 900 m yr^{-1} from December 2005 to February 2007, a time when two large subglacial lakes in the zone of converging flow were draining, producing a flood of water that would have reduced ice-bed coupling beneath Byrd Glacier during this time. Previous attempts to model basal thermal conditions along Byrd Glacier led to the conclusion that the bed was largely or wholly frozen, a condition that would prevent drainage of these lakes [*Scofield*, 1988; *Scofield et al.*, 1991; *Whillans et al.*, 1989; *Van der Veen*, 1999, p. 43]. Using a holistic approach, *Reusch and Hughes* [2003] calculated a "floating fraction" of ice that decreased from 1.0, where Byrd Glacier became fully afloat, in an irregular way to a minimum of 0.4 near the fjord headwall, before climbing to 0.6 in the zone of converging flow where the subglacial lakes were located.

[3] We review the database for Byrd Glacier and previous modeling approaches. Then we further develop the modeling approach by *Reusch and Hughes* [2003] that showed the most promise for allowing subglacial lake drainage. We apply the treatment to Byrd Glacier and the findings by *Stearns et al.* [2008]. We conclude with recommendations for future research.

2. Background

[4] Byrd Glacier was recognized as an important ice stream because of its size and velocity [*Swithinbank*, 1963], relatively simple geometry [*Hughes*, 1977], and proximity to McMurdo Station, the hub of American logistical operations in Antarctica (Figure 1). *Swithinbank* [1963] used surface surveying techniques and aerial photogrammetry to map a longitudinal velocity profile across the floating part of Byrd Glacier. These techniques were then employed along the full length of Byrd Glacier; the zone of converging flow at it is head and where it merged with Ross Ice Shelf at its foot [*Hughes and Fastook*, 1981]. Surveying stations were located along the fjord walls and artificial surveying targets were placed on the glacier. Fixed and moving targets were observed in aerial photos. The surface survey located a narrow grounding zone halfway up the fjord, across which tidal motion vanished. The aerial photogrammetric survey measured 1467 ice elevations and 601 ice velocities from moving patterns of surface crevasses [*Brecher*, 1986]. Velocity data showed that side drag increased from a minimum as ice entered the fjord to a maximum halfway to the ungrounding

[1]Department of Earth Sciences, Climate Change Institute, University of Maine, Orono, Maine, USA.
[2]Department of Computer Sciences, Climate Change Institute, University of Maine, Orono, Maine, USA.

0148-0227/11/2010JF001896

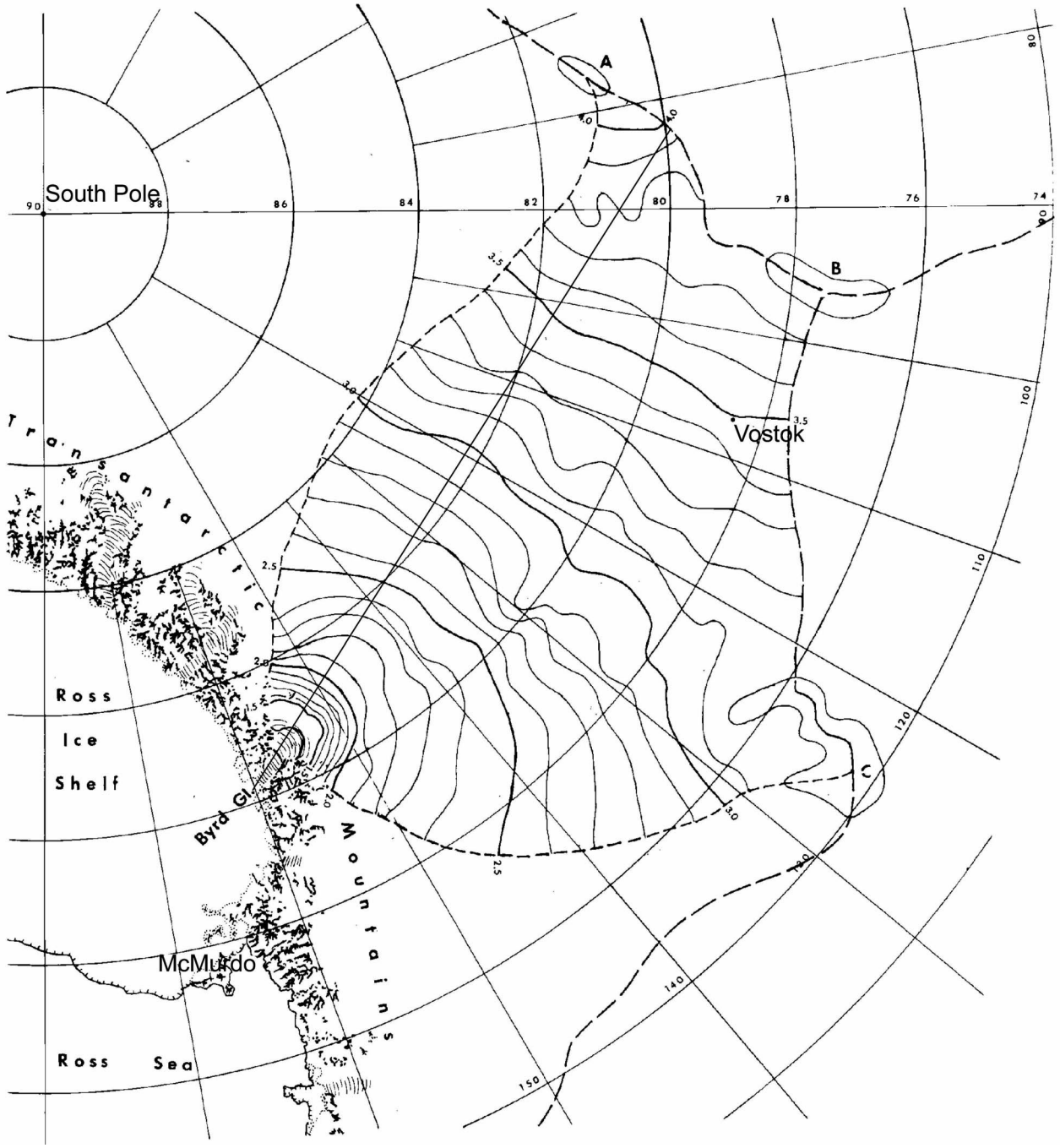

Figure 1. The ice catchment area of Byrd Glacier in East Antarctica. The ice elevation contour interval is 0.1 km. BEDMAP surface and bed profiles are used along the flowline/flowband shown. Modified from *Drewry* [1983] [see *Hughes*, 1998, Figure 3.35].

line/zone, and then vanished along lateral rifts where Byrd Glacier was decoupled from Ross Ice Shelf [*Whillans et al.*, 1989; *Zhao*, 1990; *Van der Veen*, 1999, Figure 3.6].

[5] Katabatic winds blowing down Byrd Glacier produce a surface "ablation" zone inside the fjord due to sublimation. Most surface meltwater refreezes in crevasses, so melting is not true ablation. Stakes close to the centerline yielded "ablation" rates that increased from 0.1 m yr^{-1} at the fjord entrance to 0.3 m yr^{-1} at the fjord exit during the 1978–1979 austral summer, with surface accumulation replacing surface "ablation" as katabatic winds died out on Ross Ice Shelf [*Hughes and Fastook*, 1981]. About halfway through the fjord, near the ungrounding line, surface ice took the appearance of a dried-out streambed, with polygonal "platforms" of ice some 10 m to 30 m across surrounded by crevasses about 20 m deep. When this ice reached the lower end of the fjord, about 50 km downstream, surface "ablation" had converted the platforms into conical hills about 5 m high and the crevasses were gone. Centerline ice velocity averaged 800 m yr^{-1} over this 50 km distance, giving a surface "ablation

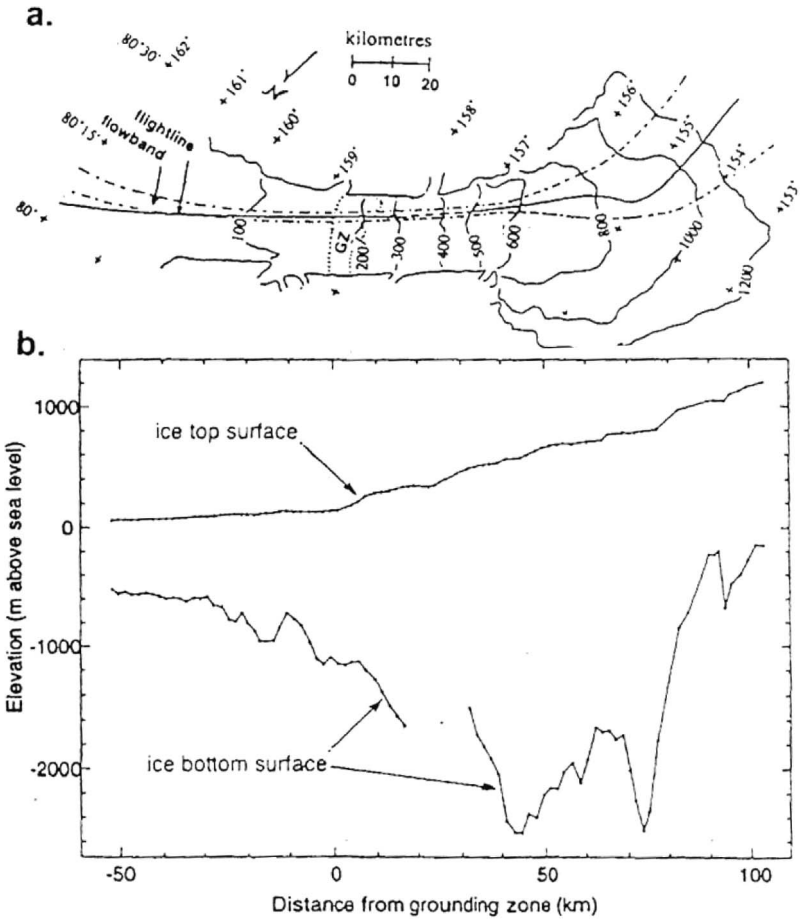

Figure 2. The only radio echo flightline giving a nearly continuous bottom reflection for Byrd Glacier. (a) The flightline (solid line) is shown in relation to a near-central ice flowband (dashed lines). GZ is the grounding zone according to *Scofield* [1988]. (b) Top and bottom reflections along the radio echo flightline [from *Reusch and Hughes*, 2003].

rate" of 20 m in 50 years, or about 0.3 to 0.4 m yr^{-1}. Basal melting rates under floating ice inside the fjord were true ablation. Using the *Brecher* [1986] data for surface velocities and elevations, and calculating ice thickness from surface elevations and the buoyancy condition for floating ice, *Kenneally and Hughes* [2004] calculated basal melting rates of 12 ± 2 m yr^{-1} over this 50 km floating length.

[6] *Scofield* [1988] and *Scofield et al.* [1991] used surface data to calculate profiles of the vertical variation of ice velocity inside an ice flowband that bracketed the radar flightline in Figure 2 along which a bed reflection was obtained. A flowband lies between adjacent flowlines, which are lines of surface ice flow drawn normal to surface elevation contour lines (see Figure 2). For ice sliding on a thawed bed, a basal melting rate of 8 ± 3 m yr^{-1} satisfied mass balance continuity. This rate is an order of magnitude higher than could be produced by a reasonable geothermal heat flux and strain heating of ice when basal sliding velocities equal measured surface velocities. For ice creeping over a frozen bed, ice velocities decrease from measured surface values to zero at the bed, depending on vertical variations of ice temperature and ice crystal orientations, both of which are unknown. However, ice warms with depth and tends to develop an "easy glide" ice fabric near a frozen bed. Vertical profiles of horizontal ice velocity were therefore constructed that preserved mass balance continuity in the flowband at distance of 4.5, 9.6, 16.5, 32, and 41 km upslope from the ungrounding line. Basal sliding velocities requiring a partly thawed bed were obtained for a linear increase of ice temperature with depth at distances of 4.5, 9.6, and 32 km. Some internal ice deformation due to creep above a frozen bed was required in addition to basal sliding on a thawed bed for mass balance continuity to be preserved at these locations. For a frozen bed with no basal sliding, ice temperatures and fabrics were adjusted within acceptable limits in order to obtain creep velocity variations that preserved mass balance continuity.

[7] *Whillans et al.* [1989] used the force-budget approach developed by *Van der Veen and Whillans* [1989a, 1989b] to calculate stresses and velocities for Byrd Glacier in three dimensions, assuming bed topography mapped along the flightline in Figure 2 did not vary laterally across the glacier. They used surface elevations and velocities mapped by *Brecher* [1986] and the flow law of ice to calculate changes in velocities and stresses with depth through the thickness of both grounded and floating ice. The gravita-

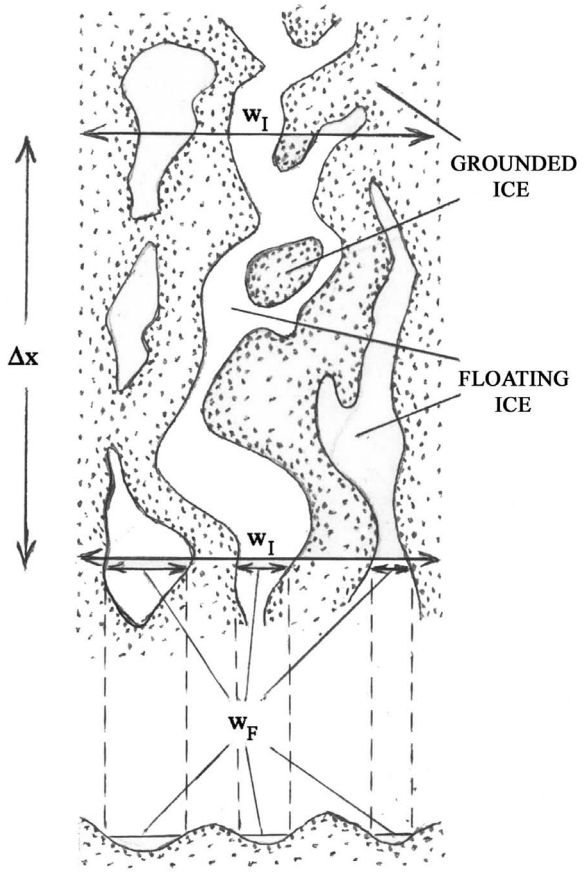

Figure 3. A cartoon of the bed under an ice stream. Ice flow is along incremental length Δx in plan view (top) and at x in transverse cross section (bottom). Ice is either floating above bedrock or supersaturated sediments and till (undotted areas) or grounded on bedrock or unsaturated sediments and till (dotted areas) for respective floating flowband widths w_F and grounded flowband widths $w_I - w_F$. Floating fraction ϕ of ice over area $w_I\Delta x$ becomes $\phi = w_F/w_I$ at x when $\Delta x \to 0$.

tional driving stress was obtained from the thickness and surface slope of ice. Surface strain rates were obtained from surface velocity gradients in both longitudinal and transverse directions. These were converted into stresses that resisted gravitational flow using the flow law. The force-budget approach allows resisting stresses to be calculated at depth, with the basal shear stress obtained from the difference between the driving stress and the sum of side shear stresses and gradients in the longitudinal and transverse axial stresses. Vertical strain rates were obtained from the incompressibility of ice, so that longitudinal, transverse, and vertical strain rates sum to zero. Ice stiffness was assumed to be constant throughout Byrd Glacier, so softening of ice caused by higher temperatures at depth and by development of "easy glide" ice fabrics caused by basal and side drag were ignored. With these constraints, results were most reliable along the flightline in Figure 2. The basal shear stress was effectively zero for floating ice, as expected, and high for grounded ice, with the highest values locating basal "sticky spots." These results indicated a bed having frozen and thawed regions, but *Van der Veen* [1999, p. 43] concluded the bed was frozen.

3. Theory

[8] Calculating a "floating fraction" along Byrd Glacier began with *Reusch and Hughes* [2003]. They employed a geometrical approach to the longitudinal force balance in the direction of ice flow that gave an ice stream "pulling power" linked to the "floating fraction" of ice [*Hughes*, 1992]. Pulling power is the product of the gravitational pulling force and the ice velocity, so it is a measure of the ability of an ice stream to downdraw interior ice. Downdraw gives ice streams their concave profile, in sharp contrast to the convex profile generated by slower sheet flow. Pulling power requires a bed similar to the one shown in Figure 3. The floating portions of ice in basal area A_I sum to give area A_F, where $A_F = 0$ when ice is fully grounded and $A_F = A_I$ when ice is fully floating. In general, these are the respective conditions for sheet flow and shelf flow, so $0 < A_F < A_I$ in streamflow represents a transition from sheet flow to shelf flow. The physical basis for a "floating fraction" is elusive. Is it parts of the bed where bedrock bumps that control basal sliding in a sliding "law" of the *Weertman* [1957a] type are drowned, parts of the bed where low places are filled with water, parts of the bed where till and sediments lose cohesion because they are supersaturated with water, or combinations of these? We do not know, but the important point is the "floating fraction" of the bed is the region where the bed provides no resistance to ice flow owing to the concentration of basal water that effectively uncouples ice from the bed.

[9] In the geometrical force balance along ice flow, floating fraction ϕ of ice is formally defined at any location x along a flowband of ice where w_F is the floating part of width w_I in Figure 3 so $\phi = A_F/A_I$ in area $A_I = w_I\Delta x$ becomes

$$\phi = \frac{w_F}{w_I} = \frac{h_F}{h_I} = \frac{(\rho_W/\rho_I)h_W}{h_I} = \frac{\rho_W g h_W}{\rho_I g h_I} = \frac{P_W}{P_I} \tag{1}$$

Here $P_W = \rho_W g h_W$ is an "effective" basal water pressure "produced" by an "effective" water height h_W above the bed that would float ice of height h_F, $P_I = \rho_I g h_I$ is basal ice pressure produced by ice height h_I above the bed, ρ_W and ρ_I are respective water and ice densities, and g is gravity acceleration. Actual basal water pressure is close to P_I, differing slightly when basal water flows from sources to sinks, so P_W in equation (1) is defined as an effective water pressure that reduces basal resistance to ice flow such that $P_W = P_I\phi$. Resistance vanishes when fully grounded ice ($\phi = 0$) becomes fully afloat ($\phi = 1$). In Figure 4, x is horizontal and positive against flow, with $x = 0$ at the ungrounding line where $\phi = 1$. An ice "flotation" height $h_F = (\rho_W/\rho_I)h_W = \phi h_I$ is the fraction ϕ of h_I that would be floated by "effective" basal water pressure P_W such that $h_F = (w_F/w_I)h_I$ at x. For ice streams it is useful to make flowband width w_I the (average) width of the ice stream, so side shear is included in the longitudinal force balance.

[10] The geometrical force balance in direction x of linear ice flow for constant flowband width w_I satisfies the equation [*Hughes*, 2009a]

$$P_I\alpha = \partial(\sigma_F h_I)/\partial x + \tau_O + 2\tau_S(h_I/w_I) \tag{2}$$

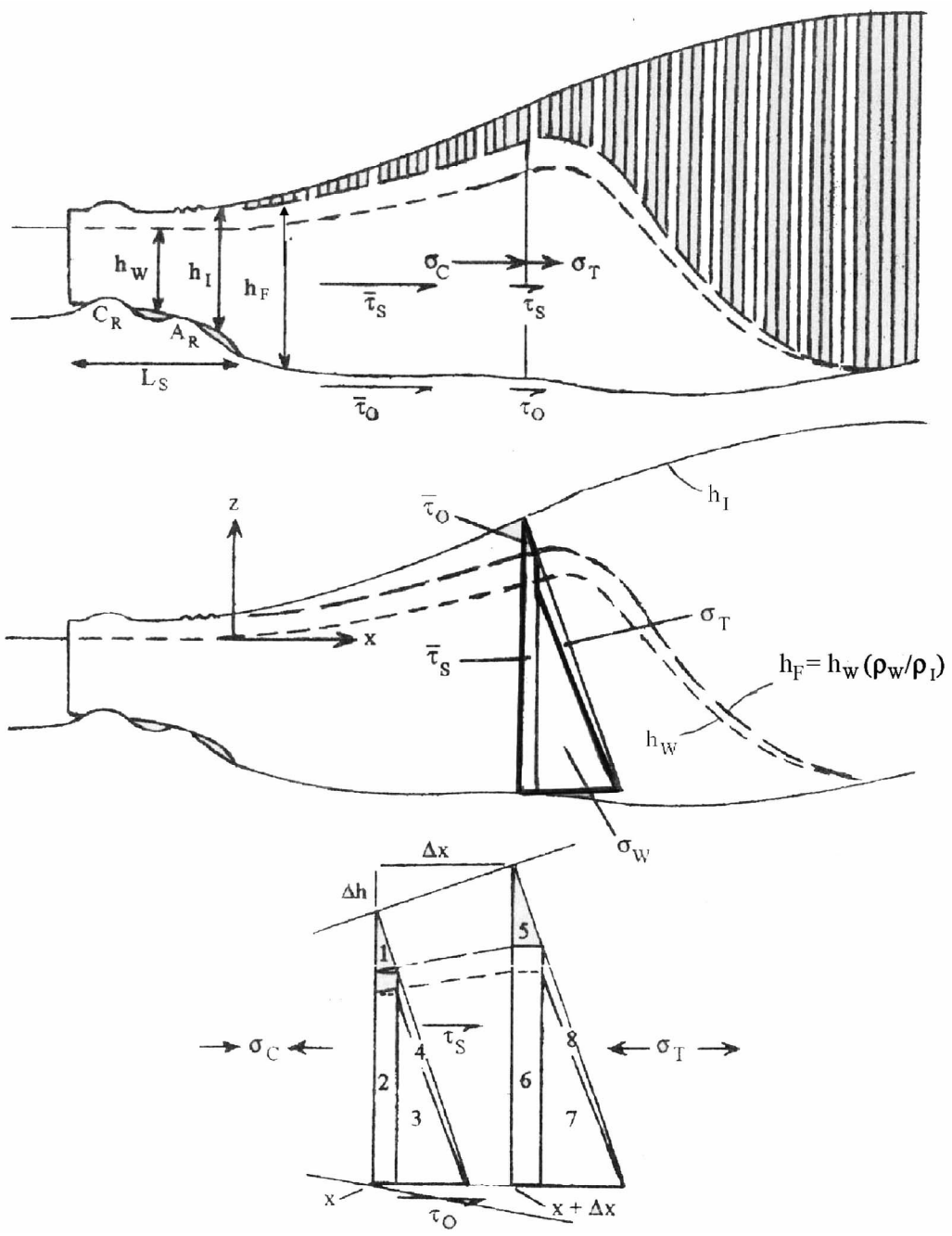

Figure 4. The geometrical force balance on an ice stream ending as a confined ice shelf. (top) Stresses that resist gravitational flow along x. The bed supports ice in the shaded area. Ice in the unshaded area is supported by "effective" basal water pressure. (middle) Gravitational forces at x represented as triangles and a rectangle are linked to specific resisting stresses. The area inside the thick border is linked to compressive stress σ_C. Heights h_I, h_W, and h_F are measured from the bed for $x > 0$. (bottom) Resisting stresses and gravitational forces along Δx. Resisting and gravitational forces are balanced along x and Δx [see *Hughes*, 2009a].

Here $P_I\alpha$ is the gravitational driving stress, α is ice surface slope, $\partial(\sigma_F h_I)/\partial x$ is the longitudinal force gradient, τ_O is the basal shear stress, and τ_S is the side shear stress, all at x. Table 1 from *Hughes* [2009a] shows how all these stresses depend on ϕ at x, where flotation stress $\sigma_F = \sigma_W + \sigma_T$ for water stress σ_W, defined by the force balance $\sigma_W h_I = \overline{P}_W h_W$, and tensile stress σ_T that provides pulling power. Here $\overline{P}_W = 1/2\ \rho_W g h_W$ is the average "effective" water pressure in "effective" water height h_W. When $\phi = 1$, $\overline{P}_W$ is the actual average water pressure and h_W is the actual water height

Table 1. Pressures and Resisting Stresses Linked to Floating Fraction ϕ of Ice and Gravitational Forces Numbered in Figure 4 for the Geometrical Force Balance[a]

	Equation
"Effective" basal water pressure at x, from gravity force 3	$P_W = \rho_W g h_W$
Ice overburden pressure at x, from gravity force (1 + 2 + 3 + 4)	$P_I = \rho_I g h_I$
Upslope tensile stress at x, from gravity force 4	$\sigma_T = \overline{P}_I(1 - \rho_I/\rho_W)\phi^2$
Downslope water pressure stress at x, from gravity force 3	$\sigma_W = \overline{P}_I(\rho_I/\rho_W)\phi^2$
Upslope flotation stress at x from gravity force (3 + 4)	$\sigma_F = \sigma_T + \sigma_W = \overline{P}_I\phi^2$
Longitudinal force balance at x from gravity force [(5 + 6 + 7 + 8) − (1 + 2 + 3 + 4)]	$P_I\alpha = \partial(\sigma_F h_I)/\partial x + \tau_O + 2\tau_S(h_I/w_I)$
Flotation force gradient at x from gravity force [(7 + 8) − (3 + 4)]	$\partial(\sigma_F h_I)/\partial x = P_I\phi(\phi\alpha + h_I\partial\phi/\partial x)$
Basal shear stress at x from gravity force (5–1)	$\tau_O = P_I(1 - \phi)^2\alpha - P_I h_I(1 - \phi)\partial\phi/\partial x$
Side shear stress at x from gravity force (6–2)	$\tau_S = P_I(w_I/h_I)\phi(1 - \phi)\alpha + \overline{P}_I w_I(1 - 2\phi)\partial\phi/\partial x$
Average downslope basal shear stress to x from gravity force 1	$\overline{\tau}_O = \overline{P}_I w_I h_I(1 - \phi)^2/(w_I x + A_R)$
Average downslope side shear stress to x from gravity force 2	$\overline{\tau}_S = P_I w_I h_I\phi(1 - \phi)/(2\bar{h}x + 2L_S\bar{h}_S + C_R\bar{h}_R)$
Downslope compressive stress at x due to $\overline{\tau}_O$ and $\overline{\tau}_S$ along x and σ_W at $x = 0$	$\sigma_C = \overline{P}_I - \sigma_T = \overline{P}_I - \overline{P}_I(1 - \rho_I/\rho_W)\phi^2$
First-order floating fraction of ice at x	$\phi = h_O/h_I$

[a]From *Hughes* [2009a].

because ice is fully afloat. Figure 5 plots the stress equations in Table 1, as fractions of P_I or $\overline{P}_I = 1/2\ P_I$, over the range $0 \le \phi \le 1$.

4. Consider a Flowband Having the Nearly Constant Width of Byrd Glacier

[11] In Figure 4 for constant w_I, flotation, water, and tensile stresses σ_F, σ_W, and σ_T, respectively, resist gravitational driving forces represented by triangular areas 3 + 4, 3, and 4, respectively, of triangular area 1 + 2 + 3 + 4 that represents total gravitational driving force $F_G = \overline{P}_I A_x$, where $\overline{P}_I = 1/2\ P_I$ is ice pressure averaged through h_I and acting on area $A_x = w_I h_I$. Compressive stress $\sigma_C = \overline{P}_I - \sigma_T$ at x resists the gravitational driving force represented by areas 1, 2, and 3. Here σ_C at x is a proxy for all downstream resistance to ice flow caused by average basal and side shear stresses $\overline{\tau}_O$ and $\overline{\tau}_S$ along x, effective and actual average basal water pressure $\overline{P}_W = \overline{P}_I$ at x = 0 where $\phi = 1$, and buttressing force F_B caused by a confined and pinned ice shelf floating beyond the ungrounding line at $x = 0$. Basal and side resisting shear stresses τ_O and τ_S at x are respectively linked to gravitational driving forces represented by the differences between areas 5 and 1 for τ_O and areas 6 and 2 for τ_S as $\Delta x \to 0$ in Figure 4. The ϕ dependence of these stresses, given in Table 1, are derived by *Hughes* [2009a].

[12] A first approximation for ϕ at x is obtained from the linear geometrical force balance alone and is [*Hughes*, 2009a]

$$\phi \approx h_O/h_I \tag{3}$$

where h_O is h_I at $x = 0$ and h_O at $x = 0$ substitutes for h_F at $x > 0$ in equation (1). In equation (3), ϕ and h_O are determined by ice-bed uncoupling beneath and beyond ice streams, respectively. An increase in h_O increases the gravitational driving force $F_G = \overline{P}_I w_I h_O = 1/2\ \rho_I g w_I h_O^2$ at $x = 0$ needed to balance "buttressing" force F_B resulting from ice-bed coupling of an ice shelf confined in an embayment, pinned to islands and shoals, or both. If the ice stream ends on land, F_B is caused by ice-bed coupling of its terminal ice lobe. Equation (3) requires a finite h_O at $x = 0$ and finite values of ϕ at $x > 0$ for stream flow. For sheet flow, $h_O = \phi = 0$ [*Hughes*, 2003, Figure 7]. For shelf flow, $h_O = h_I$ and $\phi = 1$ [*Weertman*, 1957b].

[13] Illustrating the gravitational driving force by the area of the big triangle at x and its change in area at $x + \Delta x$ in Figure 4 (bottom) in the longitudinal force balance requires assigning resisting forces and their associated stresses to specific areas of the big triangles: $\overline{\tau}_O$ to triangle 1, τ_O to triangle 5 minus triangle 1, $\overline{\tau}_S$ to rectangle 2, τ_S to rectangle 6 minus rectangle 2, σ_T to triangle 4, σ_W to triangle 3, and σ_C to the sum of triangle 1, triangle 3, and rectangle 2, so that $\overline{P}_I = \sigma_T + \sigma_C$ at x. Here $\overline{\tau}_O$ and $\overline{\tau}_S$ are τ_O and τ_S averaged downstream from x. Sectioning the large triangle at x in Figure 4 (middle) and Figure 4 (bottom) into smaller triangles 1, 3, and 4, and rectangle 2, in this way shows that

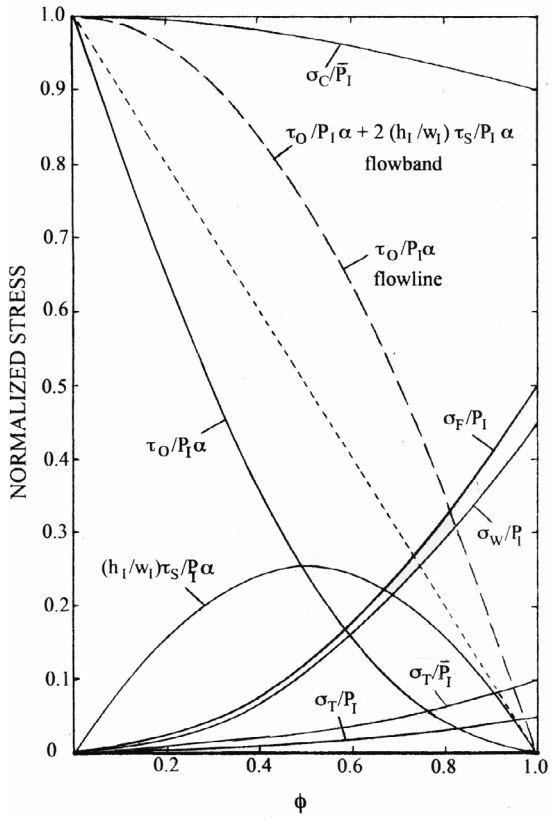

Figure 5. Plots of the stress equations in Table 1 over the range $0 \le \phi \le 1$.

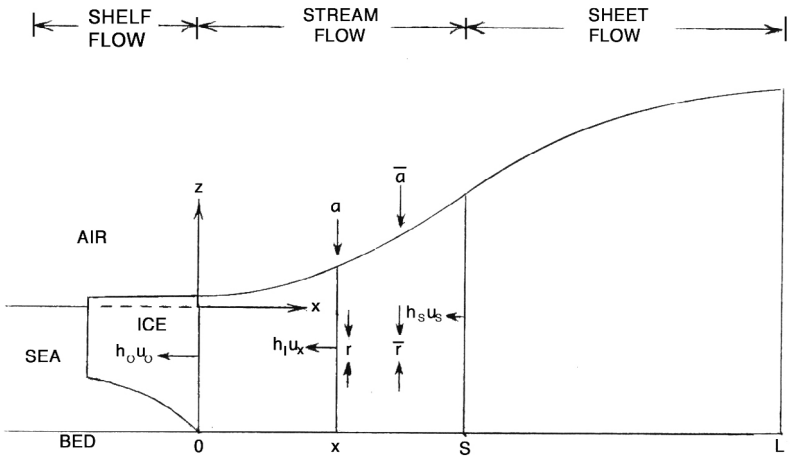

Figure 6. A longitudinal profile of an ice sheet flowband of constant width showing components of the mass balance for sheet, stream, and shelf flow from right to left. Ice thickness h_I and mean ice velocity u_x are shown at x positions 0, x, S, and L for mean accumulation rate $\overline{a}$ and ice thinning rate $\overline{r}$ averaged along x and rates a and r at x.

σ_T "pulls" upstream ice, whereas σ_C "pushes" downstream ice and is a proxy for all downslope resistance to ice flow, specifically downslope resistance from basal drag causing $\overline{\tau}_O$, resistance from side drag causing $\overline{\tau}_S$, resistance due to mean water pressure $(\overline{P}_W)_O$ at $x = 0$, and resistance due to a buttressing ice shelf caused by side grounding along length L_S and basal grounding beneath ice rises of circumference C_R and ice rumples of area A_R in Figure 4 (top). Figure 4 also shows that $\sigma_C = \sigma_W$ at $x = 0$, where $\sigma_W h_O = \overline{P}_W h_W$.

[14] Equation (3) is obtained by balancing the gravitational force with resisting forces: basal and side drag along x, water buttressing at $x = 0$, and ice-shelf buttressing beyond the ice stream. The greater the resistance the higher h_I becomes, and the greater the buttressing the higher h_O becomes. Equation (3) provides a "snapshot" of ice-bed coupling linked to ϕ at any location x along a flowband. To obtain a "motion picture" over time, the force balance must be combined with the mass balance [*Hughes*, 2009b]. This is now done.

5. Formulating the Mass Balance

[15] A more accurate determination of ϕ variations along x is obtained by combining the linear force balance with a linear mass balance, so the "defining" equation for ϕ, equation (1), replaces equation (3) as the "working" equation. Figure 6 shows the mass balance for a linear ice stream that lies on a horizontal bed and supplies a floating ice shelf, both of constant width w_I, with $x = 0$ at the (un)grounding line where $h_I = h_O$ is ice thickness and u_O is ice velocity, and x is positive upstream where ice thickness is h_I and ice velocity is u_x. Average ice surface accumulation rate $\overline{a}$ and ice creep thinning rate $\overline{r}$ along x are obtained from know rates a and r at x. As shown by Figure 6, the mass balance equation for ice flow beginning at $x = L$ where $h_I = h_L$ and $u_x = u_L = 0$ is

$$(\overline{a} - \overline{r})(L - x) = h_I u_x \tag{4}$$

All quantities in equation (4) are positive.

[16] Ice streams have wet beds that allow basal sliding. Ice sheet models generally "tune" a sliding velocity to satisfy mass balance continuity in equation (4). We obtain mass balance continuity separately for grounded sheet flow ($\phi = 0$) and floating shelf flow ($\phi = 1$) and then use floating fraction ϕ as our tuning parameter for streamflow ($0 < \phi < 1$). Consider linear sheet flow using the *Weertman* [1957a] sliding "law" for grounded ice at x that links basal shear stress τ_O to sliding velocity u_S as follows:

$$u_x = u_S = (\tau_O/B)^m = (\rho_I\ g\ h_I\ \alpha/B)^m \tag{5}$$

where τ_O is equated with the gravitational driving stress $P_I\alpha$ for ice surface slope α in sheet flow, B is a sliding parameter that can be tuned to satisfy mass continuity by specifying a variable but unknown bed roughness, and $m = 1/2\ (n + 1) = 2$ is a sliding exponent linked to viscoplastic exponent $n = 3$ in the flow law for creep of ice. For stream flow, equation (5) is modified to replace B with ϕ as the tuning parameter. For sheet flow, substituting equation (5) for u_x in equation (4) and solving for α when $dh/dx = dh_I/dx$ for ice height h above sea level and height h_I above a flat horizontal bed:

$$\alpha = \frac{dh_I}{dx} = \frac{B[(\overline{a} - \overline{r})(L - x)]^{1/m}}{\rho_I g h_I^{1+1/m}} \tag{6}$$

Integrating equation (6) for $h_I = h_O$ at $x = 0$ and h_I at $x > 0$ when B is constant because ϕ will be our tuning parameter for ice streams:

$$\frac{\rho_I g\left[h_I^{2+1/m} - h_O^{2+1/m}\right]}{2 + 1/m} = \frac{B(\overline{a} - \overline{r})^{1/m}\left[(L - x)^{1+1/m} - L^{1+1/m}\right]}{-(1 + 1/m)} \tag{7}$$

Solving for h_I at x:

$$h_I = \left\{h_O^{\frac{2m+1}{m}} + \left(\frac{2m+1}{m+1}\right)\frac{B(\overline{a} - \overline{r})^{1/m}}{\rho_I g}\left[L^{\frac{m+1}{m}} - (L - x)^{\frac{m+1}{m}}\right]\right\}^{\frac{m}{2m+1}} \tag{8}$$

Basal shear stress τ_O linked to surface slope α_G for grounded ice is obtained from equations (6) and (8):

$$\tau_O = \rho_I g h_I \alpha_G = \left[B/h_I^{1/m}\right][(\overline{a}-\overline{r})(L-x)]^{1/m} \tag{9}$$

Substituting equation (8) for h_I into equation (9) gives τ_O for ice grounded on a flat horizontal bed. Solving for ice surface slope $\alpha_G = (dh_I/dx)_G$ gives α_G along x without h_I:

$$\alpha_G = \left(\frac{dh_I}{dx}\right)_G = \frac{\tau_O}{\rho_I g h_I} = \frac{(B/\rho_I g)[(\overline{a}-\overline{r})(L-x)]^{1/m}}{\left\{h_O^{\frac{2m+1}{m}} + \left(\frac{2m+1}{m+1}\right)\frac{B(\overline{a}-\overline{r})^{1/m}}{\rho_I g}\left[L^{\frac{m+1}{m}} - (L-x)^{\frac{m+1}{m}}\right]\right\}^{\frac{m+1}{2m+1}}} \tag{10}$$

[17] Now consider linear shelf flow using the flow law for floating ice at x. For shelf flow extending between $x = S$ where $h_I = h_S$ and $u_x = u_S$ to $x = 0$ where $h_I = h_O$ and $u_x = u_O$, the mass balance equation from Figure 6 is

$$(\overline{a}-\overline{r})(S-x) = h_I u_x - h_S u_S \tag{11}$$

Writing equation (11) so $(a - r)$ at x replaces $(\overline{a} - \overline{r})$ averaged along x:

$$(a-r) = \partial(h_I u_x)/\partial x = h_I \partial u_x/\partial x + u_x \partial h_I/\partial x = h_I \dot{\varepsilon}_{xx} + u_x \alpha_F \tag{12}$$

Here $\dot{\varepsilon}_{xx} = \partial u_x/\partial x$ is the longitudinal strain rate and $\alpha_F = (\partial h_I/\partial x)_F$ is the ice thickness gradient for floating ice. Combining equations (11) and (12), and solving for α_F at x for floating ice:

$$\alpha_F = \left(\frac{dh_I}{dx}\right)_F = \frac{(a-r) - h_I \dot{\varepsilon}_{xx}}{u_x} = \frac{h_I(a-r) - h_I^2 \dot{\varepsilon}_{xx}}{h_s u_s + (\overline{a}-\overline{r})(S-x)} \tag{13}$$

Strain rate $\dot{\varepsilon}_{xx}$ is linked to tensile "pulling" stress σ_T through the flow law of ice for linear flow in ice floating above the bed [*Weertman*, 1957b]:

$$\dot{\varepsilon}_{xx} = \left(\tau^{n-1}/A^n\right)\sigma'_{xx} = R(\sigma'_{xx}/A)^n = (\sigma_T/2A)^n \tag{14}$$

where τ is the effective stress, A is an ice hardness parameter, n is a viscoplastic exponent, σ'_{xx} is the longitudinal deviator stress, and R is a scalar that converts τ into strain rate ratios. Taking x horizontal against ice flow, y horizontal transverse to flow, and z vertical and positive upward, linear flow in floating ice requires that $\dot{\varepsilon}_{xy} = \dot{\varepsilon}_{xz} = \dot{\varepsilon}_{yy} = 0$ and $\dot{\varepsilon}_{xx} = \dot{\varepsilon}_{yy} = \dot{\varepsilon}_{zz} = 0$ for incompressible ice. Then [*Hughes*, 1998, pp. 169–170],

$$R = \left[1 + \left(\dot{\varepsilon}_{yy}/\dot{\varepsilon}_{xx}\right) + \left(\dot{\varepsilon}_{yy}/\dot{\varepsilon}_{xx}\right)^2 + \left(\dot{\varepsilon}_{xy}/\dot{\varepsilon}_{xx}\right)^2 + \left(\dot{\varepsilon}_{xz}/\dot{\varepsilon}_{xx}\right)^2\right]^{\frac{n-1}{2}} = 1 \tag{15}$$

$$\sigma_T = \sigma_{xx} - \sigma_{zz} = \left(\sigma'_{xx} + \overline{P}_I\right) - \left(\sigma'_{zz} + \overline{P}_I\right) = \sigma'_{xx} - \sigma'_{zz} = \sigma'_{xx} + \left(\sigma'_{xx} + \sigma'_{yy}\right) = 2\sigma'_{xx} \tag{16}$$

The longitudinal force balance for ice thickness h_I floating in water of depth h_W and density ρ_W and buttressed by force $\sigma_B h_I$ because partial grounding causes tensile stress σ_T to be partly overcome by back or buttressing stress σ_B at $x = 0$ where $h_I = h_O$ and $\rho_I h_I = \rho_W h_W$:

$$\sigma_T h_I = \left(\overline{P}_I h_I - \overline{P}_W h_W\right) - \sigma_B h_O = {}^1\!/_2\ \rho_I g h_I^2 - {}^1\!/_2\ \rho_W g h_W^2 - \sigma_B h_O = {}^1\!/_2\ \rho_I g h_I^2 (1 - \rho_I/\rho_W) - \sigma_B h_O \tag{17}$$

Solving for longitudinal pulling stress σ_T that gives longitudinal strain rate $\dot{\varepsilon}_{xx}$:

$$\sigma_T = {}^1\!/_2\ \rho_I\ g\ h_I(1 - \rho_I/\rho_W) - \sigma_B \tag{18}$$

Since σ_B is determined at $x = 0$ where $h_I = h_O$:

$$\sigma_B = f_B\left[{}^1\!/_2\ \rho_I\ g\ h_O(1 - \rho_I/\rho_W)\right] \tag{19}$$

Here f_B is a buttressing fraction such that $f_B = 0$ for no buttressing and $f_B = 1$ for full buttressing. Using equations (14) through (19) to get $\dot{\varepsilon}_{xx}$, equation (13) is solved to get ice thickness gradient $\alpha_F = (dh_I/dx)_F$ for ice floating just above a flat horizontal bed:

$$\alpha_F = \left(\frac{dh_I}{dx}\right)_F = \left[\frac{h_I(a-r) - h_I^2[(\rho_I g/4A)(1 - \rho_I/\rho_W)(h_I - f_B h_O)]^n}{h_S u_S + (\overline{a}-\overline{r})(S-x)}\right] \tag{20}$$

[18] Now consider streamflow at x using floating fraction ϕ as a "tuning parameter" to satisfy mass balance continuity. From Table 1, ignoring terms containing $\partial\phi/\partial x$, the longitudinal force balance given by equation (2) applied to ice streams, along which $0 < \phi < 1$, is satisfied when:

$$\overline{P}_I = {}^1\!/_2\ P_I = {}^1\!/_2\ \rho_I\ g\ h_I \tag{21}$$

$$\sigma_F = \sigma_W + \sigma_T = \overline{P}_I(\rho_I/\rho_W)\phi^2 + \overline{P}_I(1 - \rho_I/\rho_W)\phi^2 = \overline{P}_I\phi^2 \tag{22}$$

$$\tau_O \approx P_I(1-\phi)^2\alpha \tag{23}$$

$$\tau_S \approx P_I(w_I/h_I)\phi(1-\phi)\alpha \tag{24}$$

$$\partial(\sigma_F h_I)/\partial x = P_I\phi^2\partial h_I/\partial x + \overline{P}_I h_I \partial\phi^2/\partial x \approx P_I\phi^2\partial h_I/\partial x \tag{25}$$

where $\partial\phi^2/\partial x = 2\phi\partial\phi/\partial x$ and terms containing $\partial\phi/\partial x$ are ignored. Substituting these equations into equation (2), with ice surface slopes $(\Delta h_I/\Delta x)_F$ for floating ice and $(\Delta h_I/\Delta x)_G$ for grounded ice both just above a flat horizontal bed, and solving over discrete surface slope $\Delta h/\Delta x$ in incremental length Δx:

$$\frac{\Delta h}{\Delta x} = \frac{\Delta(\sigma_F h_I)/\Delta x}{P_I} + \frac{\tau_O}{P_I} + \frac{2\tau_S(h_I/w_I)}{P_I} = \phi^2\left(\frac{\Delta h_I}{\Delta x}\right)_F + (1-\phi)^2\left(\frac{\Delta h_I}{\Delta x}\right)_G + 2\phi(1-\phi)\frac{\Delta h}{\Delta x} \tag{26}$$

where h is ice height above sea level and h_I is ice height above the bed.

[19] Equation (2) is valid in general for linear flow, so equation (26) applies for variable bed topography. Let the bed be represented by an up-down staircase, with ice columns having incremental horizontal length Δx on steps, so that $\Delta h/\Delta x = \Delta h_I/\Delta x$. Then changes in bed depth below sea level or height above sea level take place between ice columns. Substituting equation (20) for $(\Delta h_I/\Delta x)_F$ where ice is floating and equation (6) for $(\Delta h_I/\Delta_x)_G$ where ice is grounded, both along an ice stream, with h_I now including bed topography, and collecting terms containing ice surface slope $\Delta h/\Delta x$:

$$\left[\frac{\Delta h}{\Delta x}\right]\left(1-2\phi+2\phi^2\right) - \left[\frac{h_I(a-r)-h_I^2[(\rho_I g/4A)(1-\rho_I/\rho_W)(h_I-f_B h_O)]^n}{h_S u_S+(\overline{a}-\overline{r})(S-x)}\right]\phi^2 - \left[\frac{\frac{B}{\rho_I g}[(\overline{a}-\overline{r})(L-x)]^{\frac{1}{m}}}{h_I^{1+\frac{1}{m}}}\right]\left(1-2\phi+\phi^2\right) = C_1\left(1-2\phi+2\phi^2\right)-C_2\phi^2-C_3\left(1-2\phi+\phi^2\right)=0 \quad (27)$$

Here C_1 through C_3 are terms in square brackets. Writing equation (27) as a quadratic equation:

$$(2C_1-C_2-C_3)\phi^2-(2C_1-2C_3)\phi+(C_1-C_3)=0 \quad (28)$$

The solutions of equation (28) are

$$\phi=\frac{(2C_1-2C_3)\pm\left[(2C_1-2C_3)^2-4(C_1-C_3)(2C_1-C_2-C_3)\right]^{1/2}}{2(2C_1-C_2-C_3)} \quad (29)$$

[20] Ice height h_I above the bed in equation (8) and ice thickness gradient dh_I/dx in equation (10), with h_O ignored, both vary with surface condition $(\overline{a}-\overline{r})$, mean accumulation minus thinning rates, raised to the 1/5 power for $m = 2$ in basal sliding equation (5). This dependence is very weak compared to the dependence on floating fraction ϕ in equation (27) and confirms the first-order condition that ice-sheet heights above the bed are determined by the strength of ice-bed coupling, quantified by the floating fraction of ice, much more than by the surface mass balance.

6. Solution for a Flowline Down the Centerline of Ice Streams

[21] Side shear stresses vanish along the centerlines of ice streams, but side drag still elevates the ice surface. The radar flightline in Figure 2 is close to the centerline of Byrd Glacier where side shear stresses vanish. The effect of side drag on elevating the ice surface can be included by modifying the geometrical longitudinal force balance so it applies along the central flowline of an ice stream. Basal shear stress τ_O is augmented to carry resistance from side shear stress τ_S because $\tau_S = 0$ along the centerline. In Figure 4 gravitational driving force F_G is the areas 5 + 6 at $x + \Delta x$ minus the areas 1 + 2 at x when side shear (6–2) is added to basal shear (5–1):

$$\begin{aligned} F_G &= (5+6)-(1+2)=[(5+6+7+8) \\ &\quad -(7+8)]-[(1+2+3+4)-(3+4)] \\ &\approx \Delta[(1+2+3+4)-(3+4)]=\Delta\left[\overline{P}_I h_I-\overline{P}_W h_F\right] \\ &\approx \Delta\left[\left(\tfrac{1}{2}\,\rho_I\, g\, h_I\right)h_I-\left(\tfrac{1}{2}\,\rho_W\, g\, h_W\right)h_F\right] \\ &\approx \Delta\left[\tfrac{1}{2}\,\rho_I\, g\, h_I^2-\tfrac{1}{2}\,\rho_I\, g\, h_I^2\,\phi^2\right]=\tfrac{1}{2}\,\rho_I\, g\,\Delta\left[h_I^2\left(1-\phi^2\right)\right] \\ &\approx \rho_I\, g\, h_I\left(1-\phi^2\right)\Delta h_I-\rho_I\, g\, h_I^2\,\phi\,\Delta\phi=F_R=\tau_O\,\Delta x \end{aligned} \quad (30)$$

where resisting force $F_R = \tau_O \Delta x$ resists F_G. Solving for τ_O,

$$\tau_O=\rho_I\, g\, h_I\left(1-\phi^2\right)\Delta h_I/\Delta x-\rho_I\, g\, h_I^2\,\phi\,\Delta\phi/\Delta x \quad (31)$$

Equation (26) now becomes, ignoring the $\Delta\phi/\Delta x$ terms,

$$\frac{\Delta h}{\Delta x}=\frac{\Delta(\sigma_F h_I)/\Delta x}{P_I}+\frac{\tau_O}{P_I}=\phi^2\left(\frac{\Delta h_I}{\Delta x}\right)_F+\left(1-\phi^2\right)\left(\frac{\Delta h_I}{\Delta x}\right)_G \quad (32)$$

Rewriting equation (32) in terms of coefficients C_1 through C_3,

$$C_1-C_2\,\phi^2-C_3(1-\phi^2)=(C_3-C_2)\phi^2-(C_3-C_1)=0 \quad (33)$$

Solving for ϕ, using the solution for which $0 \le \phi \le 1$,

$$\phi=\pm\left(\frac{C_3-C_1}{C_3-C_2}\right)^{1/2} \quad (34)$$

7. Applications to Byrd Glacier

[22] In applying equations (29) and (34) to Byrd Glacier, we first show that surface profiles produced by specified ϕ variations along a flat horizontal bed can be used as input to get the same ϕ variations as output. Then we apply these equations to published surface and bed topography to calculate the actual ϕ variations. Two data sets are used, BEDMAP data from the grounding line to the ice divide, and radar data for Byrd Glacier itself that has higher resolution.

[23] We produced our test solution of equations (29) and (34) for a flat horizontal bed, using selective data from Byrd Glacier. At the ungrounding line where shelf flow begins, $x = 0$, $h_O = 1.3$ km, and $u_O = 820$ m yr^{-1}. Streamflow begins at $x = S$ where $h_I = h_S$ and $u_x = u_S = u_O$ (h_O/h_S) for steady state flow. Sheet flow begins at the ice divide, where $x = L = 1250$ km, $h_L = 3$ km, and $u_L = 0$. Values of h_O, u_O, and L are those for the Byrd Glacier ice drainage system. Constant quantities in equation (29) are $g = 9.81$ m s^{-2}, $A = 8$ bars yr$^{1/3}$ = 250 MPa s$^{1/3}$, $n = 3$, $B = 0.02$ bar yr$^{1/2}$ m$^{-1/2}$, $m = 2$, $\rho_I = 917$ kg m^{-3}, and $\rho_W = 1028$ kg m^{-3} for seawater.

[24] Flowband width $w_I \approx 25$ km across Byrd Glacier does not appear in equation (29), but w_I is needed to obtain $(\overline{a}-\overline{r})$ and $(a-r)$. The ice drainage system for Byrd Glaciers is 115×10^4 km^2 in area, and begins at an ice divide that connects

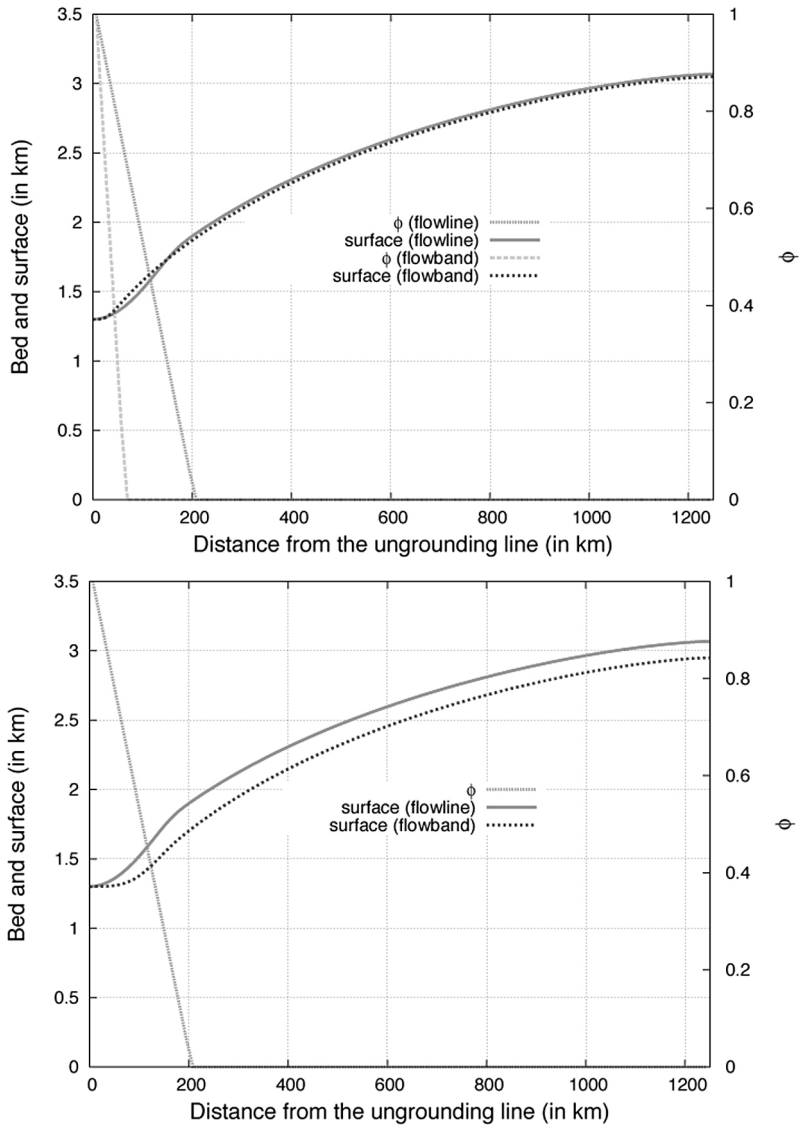

Figure 7. A test solution of equations (29) and (34) for floating fraction ϕ of ice decreasing linearly from $\phi = 1$ at $x = 0$ to $\phi = 0$ at $S \le x \le L$ in Figure 6 for ice flowing over a flat horizontal bed. Variations ϕ (solid line) produce the ice surface (dashed curve) that, in turn, produces the ϕ variation. (top) Comparing a flowband profile using equation (29) and $S = 60$ km with a flowline profile using equation (34) and $S = 200$ km. (bottom) Comparing profiles using $S = 200$ km.

three ice domes in East Antarctica (see Figure 1). Ice crosses the ungrounding line at a flux $u_O w_O h_O = 26.6$ km^3 yr^{-1}. The average ice thickening rate from ice accumulation rates and ice thinning rates is $(\overline{a} - \overline{r}) = (26.6 \text{ km}^3 \text{ yr}^{-1})/(115 \times 10^4 \text{ km}^2) = 23 \times 10^{-3}$ m yr^{-1}. A flowband 25 km wide and 1250 km long has area 3.12×10^4 km^2. The ice thickening rate in equation (29) for all ice confined to the flowband is $(\overline{a} - \overline{r}) = (a - r) = (23 \times 10^{-3} \text{ m yr}^{-1})\,[(115 \times 10^4 \text{ km}^2)/(3.12 \times 10^4 \text{ km}^2)] = 0.85$ m yr^{-1}.

[25] Figure 7 is a plot of h_I along x obtained from equations (29) and (34) for a flat horizontal bed. In Figure 7 (top), ϕ decreases linearly from $\phi = 1$ at $x = 0$ to $\phi = 0$ at $x = S = 200$ km for the flowband and at $x = S = 60$ km for the flowline. Then the two ice surface profiles mostly coincide. In Figure 7 (bottom), $x = S = 200$ km in both cases, and results in a lower flowband profile. Ice velocity decreases after it crosses the ungrounding line halfway up Byrd Glacier fjord, and then increases after ice leaves the fjord [*Brecher*, 1986]. Therefore, side drag is against the fjord walls and the inertia of Ross Ice Shelf buttress ice crossing the ungrounding line. For example, buttressing fraction $f_B = 0.765$ gave $\phi = 1$ at $x = 0$ in equation (29). The ice surface profile is concave almost to $x = S = 200$ km and convex onward to the ice divide, with $\phi = 0$ for $S \le x \le L$. Using ice height h_I above the bed calculated from equation (29) for the flowband using this ϕ variation, the identical ϕ variation is retrieved. However, 20,000 Δx steps are required to remove a "spike" in ϕ at the surface inflection line for the flowline because here $C_3 - C_2$ in equation (34) is very small (see Figure 8).

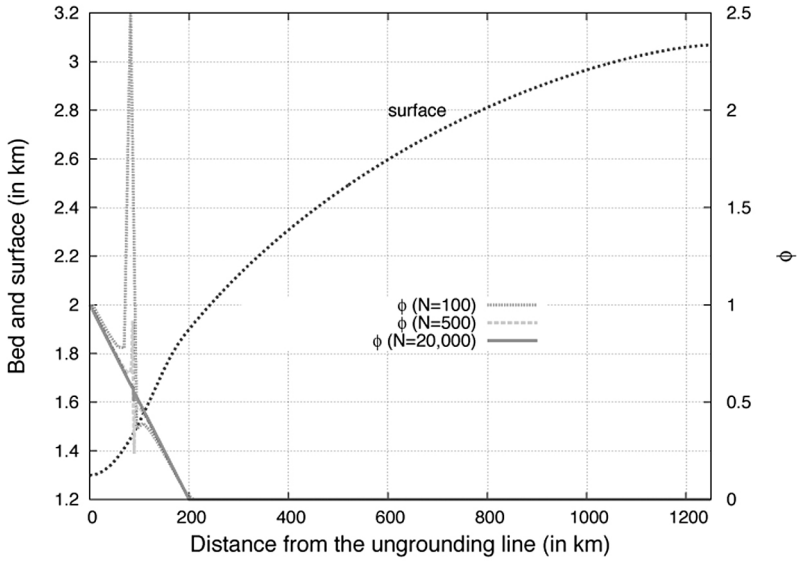

Figure 8. Reproducing the linear decrease in ϕ from the flowline profile in Figure 7. A "spike" in ϕ at $x \approx 80$ km, near the surface inflection point where $C_3 - C_1$ is small in equation (34), is removed when number N of steps is increased from 100 to 20,000.

Obtaining a concave ice surface by decreasing ϕ along x, and then retrieving ϕ from the ice surface, gives us confidence in equations (29) and (34), especially equation (29), which includes side shear.

[26] Applying equations (29) and (34) to a flowband or flowline in the Byrd Glacier ice drainage system shown in Figure 1 is confronted with two conflicting data sets, one for Byrd Glacier itself, shown in Figure 2 along the central portion of the glacier, and one shown in Figure 9 using BEDMAP data along the flowline in Figure 1 from the ungrounding line of Byrd Glacier to the East Antarctic ice divide (h_O = 463 m, L = 1352 km, and h_L = 3255 m). The subglacial lakes begin at $x = S \approx 200$ km, where h_S = 1.7 km and $u_S = u_O\,(h_O/h_S)$. When they drained, velocity u_O at $x = 0$ increased from 820 m yr^{-1} to 900 m yr^{-1} [*Stearns et al.*, 2008]. Figure 9 shows how ϕ changes along x, using equation (29) and the BEDMAP data for surface and bed profiles. Two variations of ϕ are shown, one for u_O = 820 m yr^{-1} and S = 200 km before the subglacial lakes drained, and one for u_O = 900 m yr^{-1} and S = 65 km after they drained. Drainage would recouple ice above the lakes to the bed, and thereby cause length S of streamflow to decrease. We took S = 65 km from the ungrounding line to the region of strongly converging ice flow above the fjord entrance. Streaming ice tributaries in this region converge to produce Byrd Glacier [*Jezek*, 2008]. Some recoupling of ice to the bed is shown by the lower ϕ variations for S = 65 km compared to S = 200 km. No data are available to show if there was a corresponding change in the ice surface elevation.

[27] Figure 10 shows how ϕ varies along x when equations (29) and (34) are solved using surface and bed reflections along the radar-sounding flightline in Figure 2. We call this the Swithinbank flightline because it was arranged by Charles Swithinbank, who participated in our 1978–1979 field investigation of Byrd Glacier [*Hughes and Fastook*, 1981]. The LC-130 Hercules aircraft flew only 100 m above the heavily crevassed ice surface to obtain the nearly continuous bed reflection in Figure 2. Surface and bed profiles over this 100 km length are significantly different from the BEDMAP profiles, and are more reliable (BEDMAP data points are 25 km apart). In Figure 10, the solid line shows variation of ϕ using equation (29) for flowbands; the dotted line shows variation of ϕ using equation (34) for flowlines. The ϕ variations along x are more "choppy," especially for the flowline solution, and include patches where $\phi \approx 0$, allowing the possibility of a frozen bed at these places. Ice-shelf buttressing at $x = 0$ is specified by $f_B = 0.507$ to give $\phi = 1$ in equations (29) and (34). In general ϕ decreases along x to minimum values in the foredeepened upper end of the fjord, and then increases to $\phi \approx 0.6$ at the top of the headwall, before dropping to $\phi \approx 0.3$ beyond the headwall. These results are compatible with the fjord headwall acting partly like a "dam" that impounds basal water in the vicinity of the subglacial lakes, which suddenly drained in 2006, as reported by *Stearns et al.* [2008]. Figure 10 was plotted using x = 463 m from the BEDMAP ungrounding line, h_O = 1283 m, u_O = 820 m yr^{-1}, S = 100 km, h_S = 1400 m, and $u_S = u_O\,(h_O/h_S)$ = 751 m yr^{-1}, putting the beginning of streamflow just beyond the fjord headwall and the fjord entrance, but short of the subglacial lakes in the vicinity 200 km < x < 250 km.

[28] Figures 9 and 10 present numerical solutions of equations (29) and (34). Although exact solutions exist using exact surface slopes α at points x along the flowline, average slopes $\Delta h/\Delta x$ were used for incremental steps of constant length Δx along x, and $\Delta h/\Delta x$ was calculated for a running mean of three steps. Results for 86 and 1275 steps from the ungrounding line to the ice divide using BEDMAP data show length Δx has no significant effect on how ϕ varies along x. Equation (34) is more sensitive than equation (29) to large local changes in surface slope unrelated to ice-bed

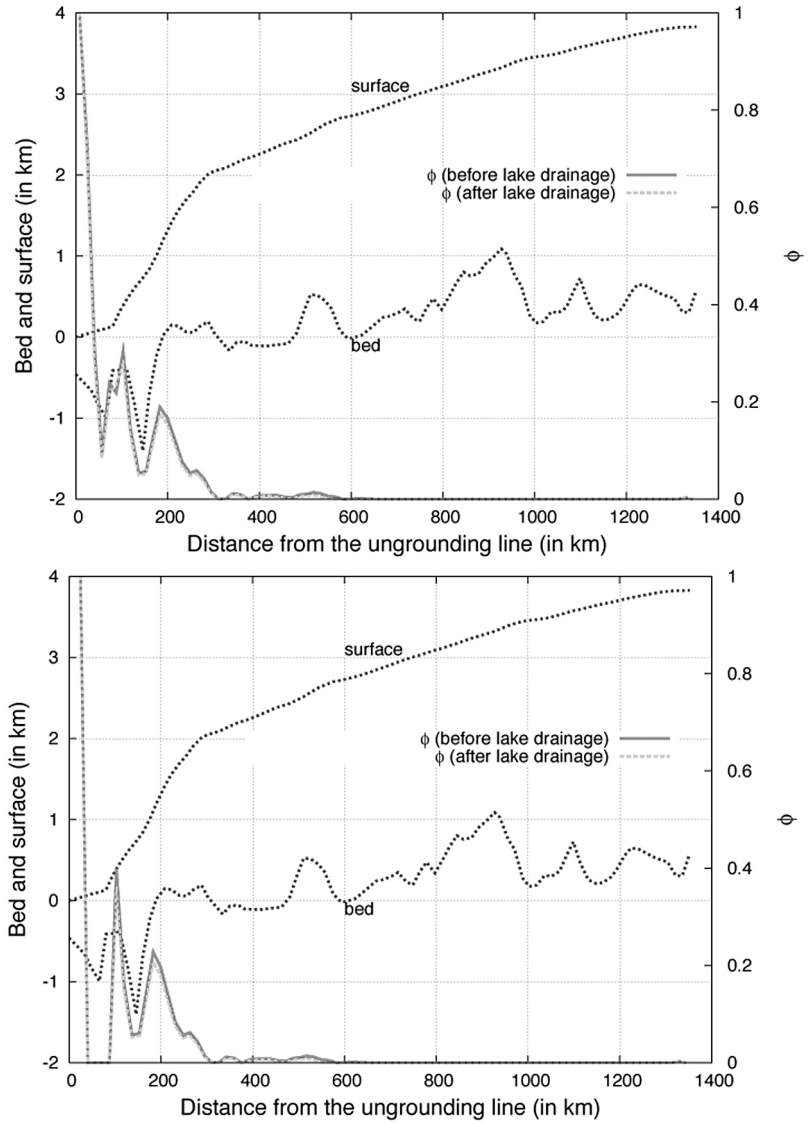

Figure 9. Variations in floating fraction ϕ along the flowband/flowline in Figure 1 before and after drainage of the subglacial lakes reported by *Stearns et al.* [2008]. Dotted lines show surface and bed profiles, solid line shows ϕ before drainage, and dashed line shows ϕ after drainage. (top) Flowband results using equation (29). (bottom) Flowline results using equation (34). Note flowline sites where ϕ exceeds the range $0 \leq \phi \leq 1$.

coupling. Not having a mechanism for these changes causes ϕ to exceed the limits $0 \leq \phi \leq 1$ at these locations.

[29] Not resolved by BEDMAP data is a series of wave-like terraces on the surface of Byrd Glacier (see Figures 2 and 10) with slopes α changing by an order of magnitude from the fronts to the tops of terraces. These major slope changes cause major changes in ϕ which may be unrelated to changes in ice-bed coupling. *Hughes* [1975] found that similar wave terraces on Meserve Glacier were produced by differential ablation rates. Higher ablation rates on the steeper sun-facing fronts of a slightly wavy surface transformed the gentle waves into relatively flat terraces separated by steep fronts. The steep wavefronts on Byrd Glacier also face the sun. If differential surface ablation rates produce the wave terraces on Byrd Glacier, it is necessary for incremental length Δx in equation (27) to "step over" regions of rapidly changing surface slope, or to employ a running mean for surface slopes so these rapid changes are smoothed. Otherwise they will cause rapid changes in ϕ that give a false record of changes in ice-bed coupling.

[30] The variation of ϕ along x in Figure 10 is similar to that found by *Reusch and Hughes* [2003], but ϕ is generally smaller. In spots $\phi \approx 0$, which is compatible with a frozen bed, but not as extensively frozen as in the studies by *Scofield* [1988], *Scofield et al.* [1991], and *Whillans et al.* [1989]. The simple first-order ϕ variations obtained from the geometrical longitudinal force balance alone [*Hughes*, 2009a], and given by equation (3), lie between the variations by *Reusch and Hughes* [2003] and the variations in Figure 10.

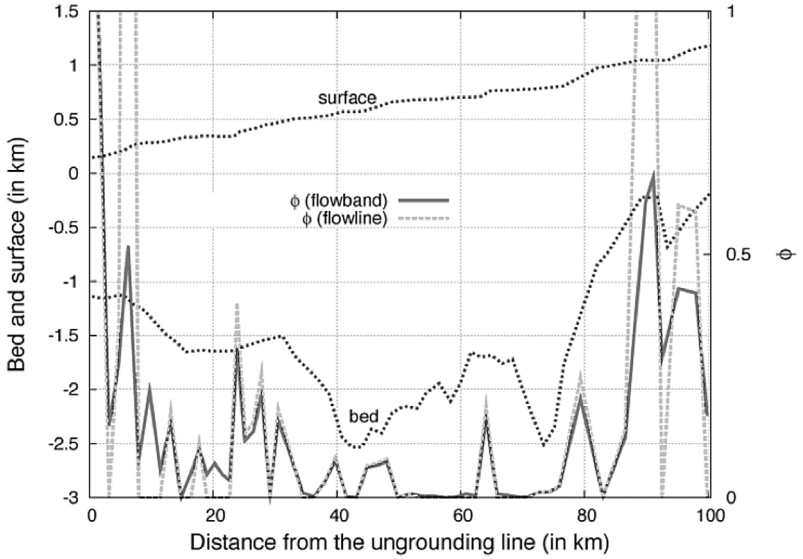

Figure 10. Variations in floating fraction ϕ along the "Swithinbank" radar flightline in Figure 2. Dotted lines are surface and bed profiles. The solid and dashed lines are ϕ variations for u_S = 751 m yr^{-1} at S = 100 km in term C_2 of equation (27) before drainage of the subglacial lakes, using equations (29) and (34). The ϕ variations along the flowline sometimes exceed the range $0 \le \phi \le 1$, as shown.

[31] The ϕ variations along x for Byrd Glacier obtained by *Reusch and Hughes* [2003] used the following expression, in which a basal sliding "law" gave $\tau_O = B\, u_S^{1/m}(1-\phi)^2$:

$$\frac{\Delta h}{\Delta x} = \frac{w_I h_I^2}{w_O h_O u_O}\left(\frac{\rho_I g h_I}{4A}\right)^n \left(1-\frac{\rho_I}{\rho_W}\right)^{n+1} \phi^{2n+2} + h_I\left(1-\frac{\rho_I}{\rho_W}\right)\phi\frac{\Delta\phi}{\Delta x} + \frac{2\tau_S}{\rho_I g w_I} + \frac{B u_S^{1/m}}{\rho_I g h_I}(1-\phi)^2 \qquad (35)$$

Equation (35) was derived by using σ_T instead of σ_F in equation (2). As seen in Table 1, this does not satisfy the longitudinal force balance given by equation (2) and introduces the quantity $(1 - \rho_I/\rho_W)$ into equation (35) at places where it does not belong. In addition, their expression for the longitudinal pulling stress was $\sigma_T = 1/2\rho_I g h_I(1 - \rho_I/\rho_W)\phi^2$ instead of equation (18), so the reduction of σ_T by σ_B was accomplished by a reduction of ϕ. However, σ_B is applied only at $x = 0$ where $\phi = 1$. Changes in ϕ occur when $x > 0$. These differences reduced $\Delta h/\Delta x$ in equation (35) by at least 90 percent, since $(1 - \rho_I/\rho_W) \approx 0.1$. Also, the dependence of $\Delta h/\Delta x$ on $C_2\phi^2$ in equation (27) is a dependence on $\phi^{2n+2} = \phi^8$ in equation (35). With $\Delta h/\Delta x \propto \phi^8$ in the first term of equation (35), the pulling power of ice streams decays much too rapidly with distance x from the ungrounding line, so it has very little reach into the ice sheet. To match the observed ice surface profile produced by the actual reach, substantially higher values of ϕ along x are required in equation (35) compared to equation (29). These flaws also appear in earlier work [e.g., *Hughes*, 1998].

[32] Ignoring terms containing $\partial\phi/\partial x$ in Table 1 was an assumption of convenience. The numerical solutions of equations (29) and (34) replaced bed topography with an up-down staircase for which changes in bed topography take place between steps. Likewise, changes in ϕ take place between steps, so that $\Delta\phi/\Delta x = 0$ on steps. This allowed equations (29) and (34) to be simple quadratic equations with equation (34) losing the ϕ dependence of τ_S when side shear is excluded. Once $\phi \to 0$, the primary mechanism for weakened ice-bed coupling is linked to the thawed fraction of an otherwise frozen bed beneath slow sheet flow [*Hughes*, 1998, chap. 3]. This treatment has been applied to sheet flow in the Byrd Glacier ice drainage system by *Wilch and Hughes* [2000].

8. Including "Floating Fraction" ϕ in Holistic Basal Sliding

[33] To complete our holistic treatment, we now derive a holistic sliding "law" for glacial ice that allows smooth transitions from slow sheet flow through fast streamflow to unconfined shelf flow. We keep the law simple so floating fraction ϕ that quantifies these transitions is the only "tuning" parameter used to satisfy mass balance continuity. These goals are attained by including ϕ in the sliding law.

[34] Glacier sliding theory was pioneered by *Weertman* [1957a, 1964] with his "tombstone" model in which bed roughness is approximated by equally spaced cubes of various sizes, and by *Lliboutry* [1958a, 1958b] who used a "washboard" bed of sinusoidal ridges and troughs transverse to ice motion. *Nye* [1969] and *Kamb* [1970] later decomposed basal structure into a roughness spectrum that could accommodate any condition of bed roughness. *Schoof and Hindmarsh* [2010] have developed a much more rigorous treatment of glacial sliding that allows variations in ice-bed coupling. We also allow these variations, but we begin with the *Weertman* [1957a, 1964] approach in which the sliding velocity is controlled by bedrock bumps of a critical size that penetrate basal ice and thereby impede slow sheet flow. We incorporate floating fraction ϕ of ice into a sliding "law" by replacing cube-shaped bumps with rectangular-based

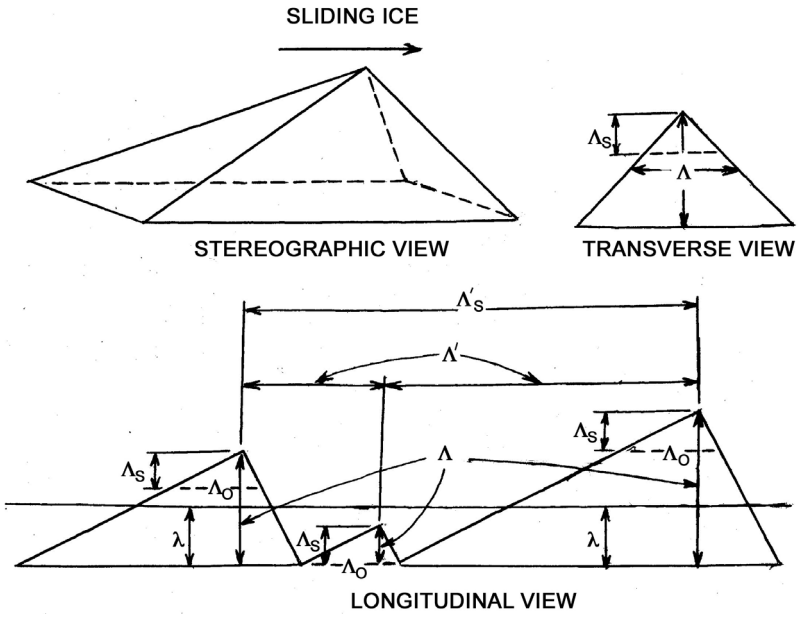

Figure 11. Basal sliding around bedrock pyramids. Sliding velocities due to equal rates of regelation and enhanced creep occurs at distance Λ_S below pyramid peaks. Mean pyramid spacing Λ' increases to Λ_S' as pyramids of various sizes are progressively submerged by basal water or supersaturated sediments and till, both of increasing thickness λ.

pyramids tilted in the direction of ice flow to account for erosion by plucking on the lee side and by abrasion on the stoss side (see Figure 11). When pyramids become progressively submerged by basal meltwater or supersaturated sediments and till that offer no resistance to ice flow, the unsubmerged pyramid cross section normal to ice flow retains the same height-to-width ratio, whereas this ratio changes for cubical bumps. This is the only reason for replacing cubes with pyramids. Submergence reduces ice-bed coupling, as quantified by ϕ.

[35] *Weertman* [1957a] found a critical bump size for cubes allowed equal rates of sliding by ice melting on the stoss side and meltwater freezing on the lee side, a process called regelation, and sliding by enhanced ice creep due to a higher ice pressure on the stoss side caused by ice motion. For bumps shaped like pyramids, the processes of regelation and enhanced creep are equal at a critical cross section between the pyramid base where enhanced creep dominates and the pyramid peak where regelation dominates (see Figure 11).

[36] Taking Λ as the average height and width of bedrock pyramids and Λ' as their average spacing, a longitudinal force balance for basal shear stress τ_O over area Λ'^2 when the bed is frozen is equated with longitudinal compressive stress σ_C over area Λ^2 normal to ice flow when the bed is thawed because then $\tau_O = 0$ and must be replaced by σ_C:

$$\tau_O \Lambda' = \sigma_C \Lambda^2 \tag{36}$$

With bumps represented by pyramids, regelation is fastest near pyramid tops where A_r is the cross-sectional area normal to ice moving in direction x and Λ_r is the mean bump length along x. Ice pushing against A_r melts due to increased basal pressure $P_O + \Delta P_O$ that reduces melting point temperature T_M by the amount

$$\Delta T_M = (\partial T_M/\partial P)\Delta P_O = C\sigma_C = C(\Lambda'/\Lambda)^2 \tau_O \tag{37}$$

where $\tau_O = P_O \alpha$ basal ice pressure P_O times ice surface slope α is the gravitational driving stress, $(\partial T_M/\partial P) = C$ is constant for small ΔT_M, and $\Delta P_O = \sigma_C$. Meltwater flows around the pyramid top, refreezes where ice pressure is reduced to $P_O - \Delta P_O$ on the lee side, and latent heat of freezing is conducted through rock distance Λ_r to provide latent heat of melting H_M. If K is the thermal conductivity of rock, so that sensible heat is conducted through Λ_r at rate $K(\Delta T_M/\Lambda_r)A_r$, regelation rate u_r is obtained by equating the rate of sensible heat conduction with rate $u_r A_r \rho_I H_M$ of latent heat production. This gives

$$u_r = \frac{K(\Delta T_M/\Lambda_r)A_r}{A_r \rho_I H_M} = \frac{K\Delta T_M}{\rho_I H_M \Lambda_r} = \frac{KC(\Lambda'/\Lambda)^2 \tau_O}{\rho_I H_M \Lambda_r} \tag{38}$$

Enhanced creep velocity u_c occurs in a volume of ice having cross-sectional area A_c normal to x and length Λ_c along x, where $\dot{\varepsilon}_c = u_c \Lambda_c$ is the compressive strain rate. Ice near the base of pyramids will be most affected by $\dot{\varepsilon}_c$. From the flow law of ice $\dot{\varepsilon}_c = (\sigma_C/A)^n$:

$$u_c = \dot{\varepsilon}_c \Lambda_c + (\sigma_C/A_M)^n \Lambda_c = \left[(\tau_O/A_M)(\Lambda'/\Lambda)^2\right]^n \Lambda_c \tag{39}$$

where A_M is the ice hardness parameter for ice at its melting point, called "temperate" ice, and n is the visco-plastic parameter for temperate ice.

[37] Notice that u_c varies directly with Λ_c, whereas u_r varies inversely with Λ_r. This means that bedrock bumps

retard sliding most for an intermediate distance Λ_O that avoids "runaway" regelation at the tops of pyramids and "runaway" enhanced creep at the bottoms of pyramids. Equating equations (38) and (39), and solving for Λ_O where $\Lambda_r = \Lambda_c$:

$$\Lambda_O = \left(\frac{\Lambda}{\Lambda'}\right)^{n-1}\left(\frac{KCA_M^n}{\rho_I H_M \tau_O^{n-1}}\right)^{1/2} \tag{40}$$

where Λ/Λ' is a "bed roughness factor" that is assumed to be constant for sheet flow. All other quantities except τ_O are constant, so Λ_O varies inversely with τ_O for $n = 3$.

[38] *Weertman* [1957a] sets sliding velocity $u_S = u_r = u_c$ but *Weertman* [1964] sets $u_S = u_r + u_c$ without explaining why. It remains unknown whether sliding velocity u_S is the sum of u_r and u_c or is equal to each one separately at Λ_O. Is u_r at the expense of u_c or not? Taking $u_S = f_S(u_r + u_c)$, where $f_S = 1$ if they are added and $f_S = 1/2$ if they are equal:

$$\begin{aligned} u_S &= f_S(u_r + u_c) = 2f_S u_r = 2f_S u_c \\ &= 2f_S\left[\left(\frac{\tau_O}{A_M}\right)\left(\frac{\Lambda'}{\Lambda}\right)^2\right]^n\left(\frac{\Lambda}{\Lambda'}\right)^{n-1}\left(\frac{KCA_M^n}{\rho_I H_M \tau_O^{n-1}}\right)^{1/2} \\ &= 2f_S\left[\left(\frac{KC}{\rho_I H_M}\right)\left(\frac{\tau_O^{n+1}}{A_M^n}\right)\right]^{1/2}\left(\frac{\Lambda'}{\Lambda}\right)^{n+1} \\ &= \left[\frac{\tau_O}{B_O(\Lambda/\Lambda')^2}\right]^{\frac{n+1}{2}} = \left(\frac{\tau_O}{B}\right)^m = \left(\frac{P_O\alpha}{B}\right)^m \end{aligned} \tag{41}$$

where $B_O = (\rho_I H_M A_M^n / 4f_S^2 KC)^{\frac{1}{n+1}}$, $B = B_O(\Lambda/\Lambda')^2$, and $m = (n + 1)/2$.

[39] Equation (41) applies for sheet flow in which basal water only wets bedrock bumps but does not drown bumps. Length Λ_O along x can also be linked to the distance Λ_S below pyramid peaks, from symmetry (see Figure 11). As basal water begins to drown the smaller pyramids, basal sliding is still resisted by larger pyramids having an undrowned height Λ_S or higher. The same applies to burial of pyramids by supersaturated sediments or till that cannot support shear stress τ_O. As this process continues in the flow direction, sheet flow becomes stream flow. Streamflow becomes shelf flow when all pyramids become drowned except for very large pyramids that produce ice rumples or ice rises on the ice shelf. Progressive drowning or burying of pyramid bumps then allows a holistic treatment of basal sliding from sheet flow to streamflow to shelf flow.

[40] As pyramids of all sizes become progressively drowned by basal water or buried by supersaturated basal sediments and till that have no shear strength, the *Weertman* [1957a] sliding mechanism can be modified to give the dependence of basal sliding on floating fraction ϕ of ice for streamflow [*Hughes*, 1998, chap. 4]. In the *Weertman* [1957a] treatment of basal sliding for sheet flow, basal water exists as a thin film that coats bedrock bumps having average height Λ and spacing Λ'. For stream flow, basal water or supersaturated sediments and till having no cohesion and thickness λ drowns or buries more bumps as λ thickens. Theories of subglacial hydrology provide a measure of λ [e.g., *Johnson*, 2002; *Johnson and Fastook*, 2002]. When bumps are pyramids and Λ_S is the distance below pyramid peaks where equal regelation and creep rates exert maximum resistance to sliding, average spacing Λ' of pyramids increases to Λ_S' as λ increases. The bed roughness factor decreases from Λ/Λ' to Λ_S/Λ_S'. Since $\Lambda - \lambda$ is the average undrowned or unburied bump height, (Λ_S/Λ_S') is an effective bed roughness factor for streamflow such that $\Lambda_S' = \Lambda'[\Lambda/(\Lambda - \lambda)]$ gives $\Lambda_S' = \Lambda'$ when $\lambda = 0$ and $\Lambda_S' = \infty$ when $\lambda = \Lambda$. Then, taking $\Lambda_S = \Lambda$ when Λ_S' becomes the variable as λ increases:

$$\frac{\Lambda_S}{\Lambda_S'} = \frac{\Lambda_S}{\Lambda'}\left(\frac{\Lambda - \lambda}{\Lambda}\right) = \frac{\Lambda}{\Lambda'}\left(1 - \frac{\lambda}{\Lambda}\right) = \frac{\Lambda}{\Lambda'}(1 - \phi)^C \tag{42}$$

where exponent c allows variations in size distributions of pyramids, $\phi = \lambda/\Lambda$, and Λ/Λ' is the bed roughness factor for sheet flow [*Weertman*, 1957a]. Keeping Λ_S constant while increasing Λ_S' is the same as keeping Λ' constant while increasing λ. Then streamflow becomes sheet flow when $\Lambda_S/\Lambda_S' \rightarrow \Lambda/\Lambda'$ as $\phi \rightarrow 0$, and streamflow becomes shelf flow when $\Lambda_S/\Lambda_S' \rightarrow 0$ as $\phi \rightarrow 1$. Basal shear stress τ_O in the *Weertman* [1957a] sliding law includes sheet flow, stream flow, and shelf flow if:

$$\begin{aligned} \tau_O &= B_O(\Lambda_S/\Lambda_S')^2 u_S^{1/m} = B_O(\Lambda/\Lambda')^2(1 - \phi)^{2C} u_S^{1/m} \\ &= B(1 - \phi)^{2C} u_S^{1/m} \end{aligned} \tag{43}$$

where B_O collects physical constants, $B = B_O(\Lambda/\Lambda')^2$ is a sliding parameter, c is a sliding exponent, $m = (n + 1)/2$ is a viscoplastic exponent that includes n in equation (39) for creep in temperate ice, and u_S is the sliding velocity.

[41] Equation (43) reduces to the *Weertman* [1957a] form when $\lambda \ll \Lambda$ is small so $\phi \ll 1$. The value of c depends on the size distribution of bumps (see Figure 12). For an ice stream, (Λ_S/Λ_S') depends on the fraction of pyramids that are at least Λ_S higher than thickness λ of basal water or supersaturated sediments and till. As thickness λ increases in Figure 12, the undrowned or unburied height $\Lambda - \lambda$ and spacing Λ_S' change slowly initially if large pyramids predominate, so $c < 1$, but the initial change is fast and $c > 1$ if small pyramids predominate. The change is linear when the size distribution is unbiased and $c = 1$. Taking $c = 1$ gives $\tau_O \propto (1 - \phi)^2$ in equation (43), just as in equation (23), so that taking $P_I = P_O$ gives

$$u_S = (P_O\ \alpha/B)^m \tag{44}$$

which is the *Weertman* [1957a] sliding law for sheet flow, $\phi = 0$, given by equation (41).

[42] Taking c = 1 gives $\tau_O \propto (1 - \phi)^2$ in equation (43), just as in equation (23). Using ϕ defined by equation (1), sliding velocity u_S in equation (43) can be written for $c = 1$, $\tau_O = P_O\alpha$, $P_O = P_I = \rho_I g h_I$, and $\phi = P_W/P_I = h_F/h_I$:

$$\begin{aligned} u_S &= \left[\frac{\tau_O}{B(1 - \phi)^2}\right]^m = \left[\frac{P_O\alpha}{B(1 - \rho_W h_W/\rho_I h_I)^2}\right]^m \\ &= \left[\frac{\rho_I g h_I \alpha}{B(1 - h_F/h_I)^2}\right] = \left[\frac{\rho_I g h_I^3 \alpha}{B(h_I - h_F)^2}\right] \end{aligned} \tag{45}$$

Here $h_I - h_F$ is ice height h_I above the bed in excess of ice height h_F that would be floated by effective water height h_W and effective basal water pressure $P_W = \rho_W g h_W$ with h_I, h_F, and h_W shown in Figure 4. Quantity $h_I - h_F$ appears in

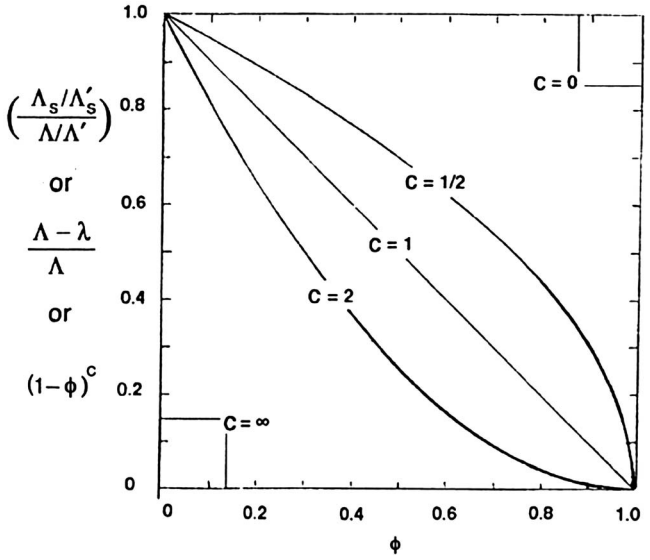

Figure 12. Extending basal sliding for sheet flow to basal sliding for stream flow. Resistance to sliding is a maximum at distance Λ_S below the peaks of bedrock pyramids in Figure 11 having average height Λ that are spaced average distance Λ' apart for sheet flow. As pyramids of variable sizes are progressively drowned by basal water or buried by supersaturated sediments or till of thickness λ, distance Λ' increases to Λ'_S. Progressive drowning or burial of pyramids (bedrock bumps) increases the floating fraction ϕ of ice such that $(\Lambda_S/\Lambda'_S)/(\Lambda/\Lambda') = (\Lambda - \lambda)/\Lambda = (1 - \phi)^C$, where $c < 1$ when large pyramids predominate, $c > 1$ when small pyramids predominate, and $c = 1$ when the size distribution is not biased.

generalized sliding laws used in ice sheet models [see *Van der Veen*, 1999, p. 77], and is deemed essential by *Lliboutry* [1968]. For sheet flow, $h_I \gg h_F$. For stream flow, $h_I > h_F$. For shelf flow, $h_I = h_F$ and $\alpha = 0$ [*Weertman*, 1957b], so equation (45) is indeterminate. Applying L'Hopital's rule, $(h_I - h_F)^2 \rightarrow 0$ faster than $\alpha \rightarrow 0$ seems possible, in which case u_S has no limiting value. None of this matters because gravitational spreading is driven by the height of ice floating above water, not α, and is resisted by a longitudinal tensile stress [*Weertman*, 1957b].

[43] Figure 4 shows how stresses in Table 1 resisting gravitational flow vary with ϕ as floating fraction $\phi = 0$ for sheet flow increases in streamflow to become $\phi = 1$ for shelf flow. All these stresses are normalized to either P_I or $\overline{P}_I = 1/2\ P_I$. Side shear stress τ_S exists only for streamflow because shelf flow is taken to be unconfined. Basal shear stress τ_O varies with $(1 - \phi)^2$ in the first approximation that ignores gradient $\partial\phi/\partial x$ along ice flow in Table 1. Then τ_O in Table 1 is τ_O given by equation (43) when $c = 1$. Two completely independent approaches both give $\tau_O \propto (1 - \phi)^2$, one when $c = 1$ for no size bias in bedrock bumps and one when $\partial\phi/\partial x$ is small enough to ignore.

9. Conclusions

[44] A geometrical force balance along flow was developed to include ice streams that discharge up to 90 percent of ice from past and present ice sheets [*Hughes*, 2009a]. This approach is based on three postulates: (1) the height of ice above the bed is determined primarily by the strength of ice-bed coupling, (2) uncoupling takes place primary along ice streams which can discharge up to 90 percent of the ice, and (3) because of the first two postulates, ice sheets are the only component of Earth's climate system that can rapidly self-destruct and thereby trigger rapid changes in climate and sea level [*Hughes*, 2009b]. The primary variable in this treatment is the floating fraction of ice along ice streams.

[45] A hypothesis based on the three postulates is applied to Byrd Glacier, the largest and fastest Antarctic ice stream supplying Ross Ice Shelf, before and after rapid drainage of two large subglacial lakes in the zone of converging flow just beyond the head of Byrd Glacier, accompanied by a ten percent increase in ice discharge velocity [*Stearns et al.*, 2008]. The geometrical force balance was applied to a simple mass balance along a flowband for Byrd Glacier. Measurable ice-bed recoupling above the lakes and decoupling downstream was obtained using the flowband and flowline models along the discharge route of flooding water. The exact discharge route is unknown because the Swithinbank flightline giving radar-derived surface and bed profiles is neither continuous nor directly intersects the subglacial lakes. Record of surface and bed profiles is along a single radar flightline that does not cross the subglacial lakes. Equation (29) and (34) can provide "motion pictures" of changing ice surfaces over time, provided that accumulation/ablation rates a and $\overline{a}$ are known so thinning/thickening rates r and $\overline{r}$ can be calculated over time. Ideally, h_I, α, and a should be determined in the map plane.

[46] *Hughes* [2009b] compares our approach with more rigorous approaches [e.g., *Marshall*, 2005; *Schoof*, 2007a, 2007b; *Sayag and Tziperman*, 2008; *Hindmarsh*, 2009; *Katz and Worster*, 2010; *Schoof and Hindmarsh*, 2010]. For Byrd Glacier, we were unable to calculate ice thinning/thickening rates r and $\overline{r}$ in equation (27) because accumulation/ablation rates a and $\overline{a}$ are unreliable. Radar mapping of basal conditions in the map plane [e.g., *Oswald and Gogineni*, 2008; *Paden et al.*, 2010] may link our floating fraction of ice to subglacial hydrology. Using floating fraction ϕ to quantify ice-bed coupling beneath ice streams might be questioned because water is in direct contact with a vertical face of ice only at the calving front of ice shelves where $\phi = 1$, so the back-pressure of water is direct, giving $\sigma_W h_I = \overline{P}_W h_W$ for back-stress σ_W in ice, see Figure 4. However, σ_W also exists at the grounding lines of ice shelves, where the buoyancy requirement $\rho_W h_W = \rho_I h_I$ still applies, so $\phi = 1$ in equation (1) even though water is no longer in direct contact with a vertical face of ice [see *Hughes*, 2009a]. Furthermore, ϕ remains just below unity hundreds of kilometers upstream from the grounding line of Whillans Ice Stream [*Engelhardt and Kamb*, 1997]. This is also the case for Kamb Ice Stream [*Robin et al.*, 1970], and for Mercer Ice Stream [*Fricker and Scambos*, 2009], observations which now span four decades. This is why these ice streams have the long concave profiles observed for linear freely floating ice shelves, for which $\phi = 1$, and not the convex profiles of ice ridges between these ice streams that are produced when ϕ decreases toward zero very quickly upslope from grounding lines[see *Hughes* [2009a, Figures 4 and 9]. These ice streams have concave profiles where they are in extending flow. Flow is resisted

mainly by longitudinal tension and side shear. Tension is inferred from the observed concave profile, whereas side shear produces a convex profile, see *Van der Veen* [1999, Figure 6.12]. Modeling Byrd Glacier or any other ice stream in the map plane faces these requirements, and these models should ideally include subglacial hydrology [e.g., *Johnson*, 2002] and all stresses that resist ice flow [e.g., *Sargent*, 2009].

[47] A sliding law of the *Weertman* [1957a] type used in equations (29) and (34) can be modified to include ϕ so the ice surface changes from convex to concave as slow sheet flow becomes fast stream flow, with ϕ used as a tuning parameter that satisfies mass balance continuity. Our sliding velocity includes resistance from a basal shear stress where ice is grounded and a longitudinal pulling stress where ice is floating, both under ice streams. These regions correspond to the thin layer of basal ice allowing two kinds of motion, slow shearing flow over a coupled bed and fast extensional flow over an uncoupled bed. Indeed, these two processes have been included in the recent sliding model by *Schoof and Hindmarsh* [2010].

[48] **Acknowledgments.** This manuscript was prepared and submitted by Beverly Hughes. Our work was supported by the NSF and NASA through a subcontract from the Center for Remote Sensing of Ice Sheets (CReSIS), University of Kansas. Two reviewers were invaluable in getting this published. Johannes Weertman and Richard Hindmarsh have encouraged our approach, with reservations. We dedicate this paper to Charles Swithinbank, who made our work possible.

References

Brecher, H. H. (1986), Surface velocity determination on large polar glaciers by aerial photogrammetry, *Ann. Glaciol.*, *8*, 22–26.

Drewry, D. J. (1983), *Antarctica: Glaciological and Geophysical Folio*, edited by D. J. Drewry, Scott Polar Res. Inst., Univ. of Cambridge, Cambridge, U. K.

Engelhardt, H., and B. Kamb (1997), Basal hydraulic system of a West Antarctic ice stream: Constraints from borehole observations, *J. Glaciol.*, *43*, 207–230.

Fricker, H. A., and T. A. Scambos (2009), Connected subglacial lake activity on lower Mercer and Whillans Ice Streams, West Antarctica, 2003–2008, *J. Glaciol.*, *55*, 303–315, doi:10.3189/002214309788608813.

Hindmarsh, R. C. A. (2009), Consistent generation of ice-stress via thermoviscous instabilities modulated by membrane stresses, *Geophys. Res. Lett.*, *36*, L06502, doi:10.1029/2008GL036877.

Hughes, T. (1975), A differential ablation-longitudinal compression mechanism for generating wave trains on cold alpine glaciers, in *Snow and Ice Symposium*, *IAHS-AISH Publ.*, *104*, 305–317.

Hughes, T. (1977), West Antarctic ice streams, *Rev. Geophys. Space Phys.*, *15*, 1–46, doi:10.1029/RG015i001p00001.

Hughes, T. (1992), On the pulling power of ice streams, *J. Glaciol.*, *38*, 125–151.

Hughes, T. (1998), *Ice Sheets*, 343 pp., Oxford Univ. Press, New York.

Hughes, T. (2003), The geometrical force balance in glaciology, *J. Geophys. Res.*, *108*(B11), 2526, doi:10.1029/2003JB002557.

Hughes, T. (2009a), Variations in ice-bed coupling beneath and beyond ice streams: The force balance, *J. Geophys. Res.*, *114*, B01410, doi:10.1029/2008JB005714.

Hughes, T. (2009b), Modeling ice sheets from the bottom up, *Quat. Sci. Rev.*, *28*, 1831–1849, doi:10.1016/j.quascirev.2009.06.004.

Hughes, T. J., and J. L. Fastook (1981), Byrd Glacier: 1978–1979 field results, *Antarct. J. US.*, *16*, 86–89.

Jezek, K. C. (2008), The Radarsat-1 Antarctic Mapping Project, *Byrd Polar Res. Cent. Rep. 22*, 64 pp., Ohio State Univ., Columbus.

Johnson, J. (2002), A basal water model for ice sheets, Ph.D. thesis, 187 pp., Univ. of Maine, Orono.

Johnson, J., and J. L. Fastook (2002), Northern Hemisphere glaciation and its sensitivity to basal melt water, *Quaternary Int.*, *95–96*, 65–74, doi:10.1016/S1040-6182(02)00028-9.

Kamb, B. (1970), Sliding motion of glaciers: Theory and observation, *Rev. Geophys.*, *8*, 673–728, doi:10.1029/RG008i004p00673.

Katz, R. F., and M. G. Worster (2010), The stability of ice-sheet grounding lines, *Proc. R. Soc. A*, *466*, 1597–1620, doi:10.1098/rspa.2009.0434.

Kenneally, J. P., and T. J. Hughes (2004), Basal melting along the floating part of Byrd Glacier, *Antarct. Sci.*, *16*, 355–358, doi:10.1017/S0954102004002068.

Lliboutry, L. (1958a), Frottement sur le lit et mouvement pas saccades d'un glacier, *C. R. Hebd. Seances Acad. Sci.*, *247*, 228–230.

Lliboutry, L. (1958b), Contribution à la théorie du frottement du glacier sur son lit, *C. R. Hebd. Seances Acad. Sci.*, *247*, 318–320.

Lliboutry, L. (1968), General theory of subglacial cavitation and sliding of temperate glaciers, *J. Glaciol.*, *7*, 21–58.

Marshall, S. J. (2005), Recent advances in understanding ice dynamics, *Earth Planet. Sci. Lett.*, *240*, 191–204, doi:10.1016/j.epsl.2005.08.016.

Nye, J. F. (1969), A calculation on the sliding of ice over a wavy surface using a Newtonian viscous approximation, *Proc. R. Soc. London, Ser. A*, *311*, 445–467.

Oswald, G. K. A., and S. P. Gogineni (2008), Recovery of subglacial water extent from Greenland radar survey data, *J. Glaciol.*, *54*, 94–106, doi:10.3189/002214308784409107.

Paden, J., T. Akins, D. Dunson, C. Allen, and S. P. Gogineni (2010), Ice-sheet bed 3-D tomography, *J. Glaciol.*, *56*, 3–11, doi:10.3189/002214310791190811.

Reusch, D., and T. J. Hughes (2003), Surface "waves" on Byrd Glacier, *Antarct. Sci.*, *15*, 547–555, doi:10.1017/S0954102003001664.

Rignot, E. J., and R. H. Thomas (2002), Mass balance of polar ice sheets, *Science*, *297*, 1502–1506, doi:10.1126/science.1073888.

Robin, G. de Q., C. W. M. Swithinbank, and B. M. E. Smith (1970), Radio-echo exploration of the Antarctic Ice Sheet, in *International Symposium on Antarctic Glaciological Exploration (ISAGE)*, *IHAS Publ.*, *86*, 97–115.

Sargent, A. (2009), Modeling ice streams, Ph.D. thesis, 106 pp., Univ. of Maine, Orono.

Sayag, R., and E. Tziperman (2008), Spontaneous generation of pure ice streams via flow instability: Role of longitudinal shear stresses and subglacial till, *J. Geophys. Res.*, *113*, B05411, doi:10.1029/2007JB005228.

Schoof, C. (2007a), Marine ice-sheet dynamics. Part 1 The case of rapid sliding, *J. Fluid Mech.*, *573*, 27–55, doi:10.1017/S0022112006003570.

Schoof, C. (2007b), Ice sheet grounding line dynamics: Steady states, stability, and hysteresis, *J. Geophys. Res.*, *112*, F03S28, doi:10.1029/2006JF000664.

Schoof, C., and R. C. A. Hindmarsh (2010), Thin-film flows with wall slip: An asymptotic analysis of higher order glacier flow models, *Q. J. Mech. Appl. Math.*, *63*(1), 73–114, doi:10.1093/qjmam/hbp025.

Scofield, J. P. (1988), Flow characteristics of an outlet glacier: Byrd Glacier, Antarctica, M.S. thesis, Univ. of Maine, Orono.

Scofield, J. P., J. L. Fastook, and T. Hughes (1991), Evidence for a frozen bed, Byrd Glacier, Antarctica, *J. Geophys. Res.*, *96*, 11,649–11,655, doi:10.1029/91JB00839.

Stearns, L. A., B. E. Smith, and G. S. Hamilton (2008), Increased flow speed on a large East Antarctic outlet glacier due to subglacial floods, *Nat. Geosci.*, *1*, 827–831, doi:10.1038/ngeo356.

Swithinbank, C. W. (1963), Ice movement of valley glaciers flowing into the Ross Ice Shelf, *Antarct. Sci.*, *141*, 523–524.

Van der Veen, C. J. (1999), *Fundamentals of Glacier Dynamics*, 462 pp., A. A. Balkema, Rotterdam, Netherlands.

Van der Veen, C. J., and I. M. Whillans (1989a), Force budget: I. Theory and numerical methods, *J. Glaciol.*, *35*(119), 53–60, doi:10.3189/002214389793701581.

Van der Veen, C. J., and I. M. Whillans (1989b), Force budget: II. Application to two-dimensional flow along Byrd Station Strain Network, Antarctica, *J. Glaciol.*, *35*, 61–67, doi:10.3189/002214389793701455.

Weertman, J. (1957a), On the sliding of glaciers, *J. Glaciol.*, *3*, 33–38.

Weertman, J. (1957b), Deformation of floating ice shelves, *J. Glaciol.*, *3*, 38–42.

Weertman, J. (1964), The theory of glacier sliding, *J. Glaciol.*, *5*, 287–303.

Whillans, I. M., Y. H. Chen, C. J. van der Veen, and T. Hughes (1989), Force Budget III: Application to three-dimensional flow of Byrd Glacier, Antarctica, *J. Glaciol.*, *35*, 68–80, doi:10.3189/002214389793701554.

Wilch, E., and T. Hughes (2000), Mapping basal thermal zones beneath the Antarctic ice sheet, *J. Glaciol.*, *46*(153), 297–310, doi:10.3189/172756500781832927.

Zhao, Z. (1990), Measurement, Analysis, and modeling of deformation of the shelf-flow, Byrd Glacier, Ph.D. thesis, Univ. of Maine, Orono.

J. Fastook and A. Sargent, Department of Computer Sciences, Climate Change Institute, University of Maine, Orono, ME 04469, USA.

T. Hughes, Department of Earth Sciences, Climate Change Institute, University of Maine, Orono, ME 04469, USA. (terry.hughes@maine.edu)